universität wien

MASTERARBEIT / MASTER'S THESIS

Titel der Masterarbeit / Title of the Master's Thesis

„Design and development of an interferometric multi-pass microscope“

verfasst von / submitted by

Jan Alexander Pac, BSc

angestrebter akademischer Grad / in partial fulfilment of the requirements for the degree of

Master of Science (MSc)

Wien, 2020 / Vienna, 2020

Studienkennzahl lt. Studienblatt / degree programme code as it appears on the student record sheet:	UA 066 876
Studienrichtung lt. Studienblatt / degree programme as it appears on the student record sheet:	Masterstudium Physik
Betreut von / Supervisor:	Ass.-Prof. Dipl.-Ing. Dr. Thomas Juffmann

Zusammenfassung

Die Erforschung der Dynamik von Proteinen ist von zentralem Interesse für die Molekularbiologie und die biomedizinische Forschung. In jüngster Zeit wurden interferometrische Bildgebungsverfahren so weit entwickelt, dass es möglich ist, die Bewegung einzelner Proteine zu beobachten. Die Sensitivität der interferometrischen Bildgebungsverfahren ist praktisch und grundlegend durch Schrotrauschen begrenzt und kann, im Prinzip, mit der Hilfe von Resonator-Techniken, wie der Multi-Pass Mikroskopie, verbessert werden. Um zu untersuchen, ob diese Verbesserung auch im Labor erreicht werden kann, haben wir ein interferometrisches Multi-Pass Mikroskop entwickelt. Der Entwicklungsprozess begann mit der Auswahl geeigneter optischer und optomechanischer Komponenten und der Konstruktion des Aufbaus innerhalb der 3D CAD Software SolidWorks. Als Nächstes wurde das Mikroskop im Labor zusammengebaut und Goldnanopartikel wurden abgebildet, um unseren Aufbau zu testen. Unsere Ergebnisse wurden mit einer theoretischen Randelementmethode (REM-Simulation oder englisch boundary element method, BEM-Simulation) überprüft. Außerdem haben wir als Machbarkeitsnachweis gezeigt, dass die interferometrische Multi-Pass Abbildung von Goldnanopartikeln einen besseren Kontrast im Vergleich zur Single-Pass Abbildung erzielt. Schließlich wurde eine Rauschanalyse des Mikroskops durchgeführt. Aufgrund dessen wurden alle Ergebnisse nochmal begutachtet und Vorschläge zur weiteren Optimierung oder Neugestaltung des Aufbaus gesammelt. Dies sollte die Richtung für zukünftige interferometrische Multi-Pass Abbildungen einzelner Proteine weisen.

Abstract

Studying the dynamics of proteins is of central interest in molecular biology and biomedical research. Recently, interferometric imaging techniques have been developed to a point where it is possible to observe the motion of single proteins. The sensitivity of interferometric imaging techniques is practically and fundamentally limited by shot noise and could, in principle, be improved using cavity enhancement techniques like multi-pass microscopy. To investigate if this improvement can also be achieved in the laboratory, we developed an interferometric multi-pass microscope. The development process began with choosing suitable optical and optomechanical components and designing the setup within the 3D CAD software SolidWorks. Next, we assembled the microscope in the laboratory and imaged gold nanoparticles to test our setup. Our findings were validated with a theoretical boundary element method (BEM) simulation. Furthermore, we demonstrated that interferometric multi-pass imaging of gold nanoparticles obtains a better contrast compared to single-pass imaging as a proof-of-concept experiment. Finally, we conducted a noise analysis of the microscope and based on the result, all findings were reviewed and suggestions on how to further optimize or redesign the setup were collected. This should lead the way for future interferometric multi-pass imaging of single proteins.

Contents

1. Introduction

Proteins are crucial components of living organisms and perform a variety of tasks within cells, ranging from DNA replication to molecular transport. Thus, molecular biology and biomedical research are highly interested in the study of protein structure and dynamics. Commonly used non-optical imaging methods like Nuclear Magnetic Resonance (NMR) spectroscopy, electron microscopy, or X-ray crystallography typically only yield static information about the structure of proteins or need high protein concentrations and ensemble averages for dynamic studies [1, 2]. In contrast, new developments in optical imaging techniques over the last decades led to a variety of methods for studying the dynamics of individual proteins and intracellular structures [3, 4, 5, 6].

1.1. Phase-contrast microscopy

In the early 1930s, Zernike revolutionized the way we look at cellular structures by inventing the phase-contrast microscope [7]. With his method, it is possible to observe transparent objects, including most cells, without the need to stain them with special dyes. This is achieved by converting phase shifts, which occur while light passes through the sample, into brightness changes which eventually lead to image contrast. Phase-contrast microscopy has traditionally mostly been used as a qualitative imaging technique. Quantitative approaches emerged only recently [8] but have not been pushed to single-molecule sensitivity.

1.2. Fluorescence microscopy

Single-molecule sensitivity was first achieved using fluorescence microscopy [6], which was established by the companies of Carl Zeiss and Carl Reichert in the early 1910s[1] [9, 10, 11, 12]. Further development by Ellinger and Hirt [9, 13] brought the imaging technique closer to today's working principle, in which molecules are labeled with a fluorescent marker, and the marker gets excited with light of a particular wavelength. Then, the marker emits fluorescent light, which is isolated and collected [14]. Sparked by the discovery and rapid exploitation of the green fluorescent protein (GFP) [15, 16, 17, 6, 3], fluorescence microscopy is nowadays used in a wide variety of different imaging techniques, with recent advances even allowing to exceed Abbe's diffraction limit [18, 19, 20, 21, 6] and the tracking of single molecules [5, 6]. Despite the tremendous successes of fluorescence microscopy, it has three inherent shortcomings [5, 22]: First, adding fluorescent markers to a biological system may change the natural behavior of the observed system. Second, the fluorescence lifetime, i.e. the time the fluorophore stays in the excited state before it emits a fluorescence photon,

[1] The company of Carl Reichert built the microscope, but it used parts that were manufactured by the company of Carl Zeiss.

fundamentally limits the achievable photon flux, which curtails the spatio-temporal resolution. Third, photobleaching and photoblinking [23] additionally decrease the photon flux and limit observation times [24].

1.3. Interferometric scattering microscopy (iSCAT)

In recent years, interferometric imaging techniques have been developed to sensitivity levels that allow the detection and tracking of single proteins [25, 26]. The developed techniques can now be seen as a valuable addition to fluorescence microscopy without having the above-mentioned shortcomings of fluorescence microscopy [22]. As a full review of the history of interferometric imaging would be beyond the scope of this thesis, I would only like to mention that a detailed history of interferometric imaging can be found in [24]. Nonetheless, a short overview of the most exciting achievements is presented below. The field of interferometric imaging is still rapidly evolving, and new applications are introduced frequently. For example, the group of Philipp Kukura recently used interferometric scattering microscopy (iSCAT) for mass determination of single biological macromolecules [27].

With the rapid emergence of new techniques and applications of interferometric imaging, a variety of different names for the associated techniques has been established. Thus, I give a brief overview of currently used techniques, their working principles, and their achievements:

- iSCAT

  The working principle of interferometric scattering microscopy (iSCAT) was first demonstrated in 2004 [28, 24] and formally established and refined in 2009 [29, 30]. Within this technique, light that is scattered by the sample interferes with unscattered light (often called 'reference light') in a stable common-path geometry[2]. For iSCAT, the microscope is typically used in reflection mode, i.e. the reference light is provided by a partial reflection at an interface (commonly between cover glass and water, in which the sample is immersed). With this configuration, the object of interest appears as a small intensity dip on top of a background. Since the signal is generated by scattered light, the technique does not need any labels.

  The groups of Philipp Kukura and Vahid Sandoghdar pioneered the development of iSCAT, and they are still the most influential contributors to the field. Both groups use iSCAT setups in reflection mode, but they have proposed and implemented several additions to the basic setup. These additions led to tremendous success in various applications: Detection of 5nm gold nanoparticles [31], detection of single unlabeled viruses [29, 32] and proteins [25, 26], single-particle tracking of gold-labeled motor proteins [4], quantitative mass imaging of macromolecules [27], observation of protein

[2] A common-path geometry is given if the scattered and reference light pass through the same optical components.

motion on a live cell membrane [33], and investigation of cell secretion processes in living cells in real-time [34]. In the last years, other research groups have also started to exploit iSCAT for new applications. For example, they were able to monitor the self-assembly of individual viral capsids [35], uncover the kinetics of DNA ejection of bacteriophages [36], and perform live-cell imaging of E. coli and yeast [37].

- COBRI

  Coherent brightfield microscopy (COBRI) can be seen as the transmission counterpart of iSCAT [38]. In the original iSCAT scheme, only a portion of the illuminating light is reflected and used as reference light. In order to avoid saturating the camera of the microscope in transmission mode, a reduction of the reference light intensity is required. Hence, a dot-shaped attenuator can be implemented in a Fourier plane after the sample[3], where the scattered and reference light are mostly spatially separated. With this setup, the group of Chia-Lung Hsieh succeeded in tracking 10 nm gold nanoparticles at 1000 frames per second [38]. They were also able to observe single viruses [40] and track native cell vesicles in live cells [41].

  In a direct comparison, i.e. integrating COBRI and iSCAT into one optical setup, it was demonstrated that the two imaging techniques have the same nanoparticle detection sensitivity at the same illumination intensity [38]. However, there are two main methodical differences between the two techniques. First, they have a different axial dependence on particle contrast. In COBRI, particle movement in the axial direction leads to a different phase evolution of scattered and reference light, which leads to a full contrast inversion (from dark to bright) over the depth of field of the microscope objective (a few micrometers for high NA objectives). In the reflection geometry of iSCAT, on the other hand, a full inversion of particle contrast already occurs over a distance of $1/4$ of the optical wavelength. Thus, continued tracking of particles is harder to achieve in iSCAT because the detection of particles is not possible if the contrast is zero. In conclusion, this means that COBRI seems to be better suited for longer tracking experiments, and iSCAT offers a higher axial localization precision [38, 40].

  Second, iSCAT is sensitive to partially reflecting interfaces of the sample. This sensitivity can be used as an advantage as it was recently demonstrated by determining the number of atomic layers of graphene with interference reflection microscopy[4] [43] and imaging the flatness of live cell membranes with iSCAT [37]. However, for tracking experiments inside cells, the sensitive interface detection can complicate continuous observation. Thus, COBRI might be better suited for observing cellular dynamics where particles get tracked inside cells [42, 38].

[3] The Kukura group implemented a similar approach of attenuating the reference light in iSCAT in [39].
[4] Interference reflection microscopy can be seen as iSCAT with a low-coherence light source [42].

- SP-IRIS

  The group of M. Selim Ünlü introduced the interferometric reflectance imaging sensor (IRIS) in 2011 as a label-free biosensor for low-cost research and clinical applications [44]. With IRIS, the object of interest is placed onto a SiO_2 layer, which was deposited on top of a silicon substrate. Next, the sample is illuminated with a multi-color LED, and the wavelength-dependant reflectivity curve is recorded. An added biomass on the oxide layer causes a shift in the reflectivity curve that can be detected. This shift can again be seen as a result of interference of reference and scattered light [45]. The imaging technique was later refined to be able to detect single nanoparticles. It was accordingly renamed to single-particle interferometric reflectance imaging sensor (SP-IRIS) [46].

  SP-IRIS operates with a partially coherent (single-color[5]) illumination LED source, which, besides its distinct reflectance geometry, sets it apart from iSCAT and COBRI. Not using a coherent laser illumination comes with certain advantages, like avoiding laser speckle and stray reflection. As a result of the reflectance geometry, particles of interest appear on the image background either as dark or bright diffraction-limited spots, depending on the focus position of the microscope objective. If one acquires images of the sample at different focus positions, the resulting defocus curves can be used for sample identification by comparing the experimentally obtained defocus curves to simulated defocus curves [48]. The oxide layer thickness in SP-IRIS can be chosen so that the forward- and backscattered light interfere constructively for a fixed illumination wavelength, which enhances the nanoparticle signal. [49].

  SP-IRIS was used to quantitatively measure bio-nanoparticle size and shape [48]. Moreover, it demonstrated reliable exosome[6] detection [52]. Ongoing efforts in virus detection led to successes in the detection and size determination of individual viruses [53], the direct detection of individual viruses in complex media [54], and automated counting and sizing of individual virions [55].

  Further improvements to the setup included limiting the illumination NA and implementing an attenuator in the Fourier plane after the sample. This improved the nanoparticle signal by a factor of 10 [49]. Additionally, the SP-IRIS community developed a technique to selectively attenuate the reference light by detecting the depolarized light from gold nanorods with a polarization microscope [47].

- SLIM

  Last but not least, the group of Gabriel Popescu has developed spatial light interference microscopy (SLIM) in 2011 [56]. SLIM is a quantitative phase imaging (QPI) tech-

[5] Typically, the illumination LED is used together with a 10 nm FWHM bandpass filter [47].

[6] Exosomes are small vesicles that are secreted by mammalian cells [50]. Recently, serious interest is directed towards them after the discovery that they are involved in intercellular communication by transferring proteins and mRNA [51, 49].

nique[7] that can easily be added to a commercially available phase-contrast microscope. Popescu et al. see SLIM as a combination of Zernike's phase-contrast microscopy [7] and Gabor's holography [57], where they want to emphasize that SLIM is capable of retrieving quantitative phase maps across the whole field of view. The quantitative phase information is generated by introducing further phase shifts after outcoupling the light from the microscope, recording the associated images, and conducting a phase estimation based on these images. SLIM was used to measure the dispersion relation associated with mass transport in live cells [58] and to detect single microtubules [59]. SLIM also shows great promise for medical diagnosis as demonstrated by identifying breast cancer tissue with high sensitivity and specificity rates in [60].

- Further techniques

  Here, I would only like to give a small chronological overview of additional interferometric imaging schemes, which are mainly adaptions or improvements of the original iSCAT scheme, and their applications. For more details about the working principles of these schemes, see the respective references. In 2009, reflection interference contrast microscopy (RICM) was used to study cell adhesion [61]. Hsieh et al. adapted iSCAT in 2014 and named it 'μs-iSCAT' to emphasize their high acquisition rate [62]. They were able to perform shot-noise limited detection of 20 nm gold particles with 2 nm spatial precision and an acquisition rate of up to 500 kHz. Next, label-free super-resolution live-cell imaging was conducted with rotating coherent scattering (ROCS) microscopy in 2016 [63]. Amplified interferometric scattering microscopy (a-iSCAT) uses wide-field illumination and an attenuation of the reference light near the back focal plane of the objective to detect small nanoparticles [64]. The sensitivity of a-iSCAT is shot-noise limited and should, in principle, be sufficient for detecting proteins as small as 15 kDa. Interferometric plasmonic microscopy (iPM) was developed in 2018 and applied to detect single exosomes [65]. Finally, Stroboscopic scattering microscopy (stroboSCAT) was used to detect charge carriers in different materials in 2019 [66].

Since all the above-mentioned methods fundamentally rely on an interferometric detection of scattered light, I am using the term 'iSCAT' in my thesis as an umbrella term for all mentioned techniques. Only if the imaging geometry is of importance, I use 'reflection iSCAT' for all iSCAT schemes that operate in reflection mode, 'COBRI' as a synonym for all interferometric transmission imaging schemes and 'SP-IRIS' for all interferometric imaging schemes that are similar to SP-IRIS, i.e. operating in reflection mode but with a reflective surface that is positioned after the sample.

All these interferometric scattering techniques are interesting for our group because they are all fundamentally [22, 30], and often also practically [25, 26, 53, 55, 62], limited by shot

[7] For details on QPI see [8].

noise, i.e. the noise that is associated with the discrete probabilistic arrival of photons at a detector and which can be modeled by a Poisson distribution [30, 67]. Thus, iSCAT could, in principle, be improved using cavity enhancement techniques like multi-pass microscopy.

1.4. Multi-pass microscopy

Multi-pass (MP) microscopy is a quantum optimal way to amplify the signal in full-field microscopy by re-imaging light onto a sample multiple times. This re-imaging, which we call 'multi-passing', enhances the contrast of the image while not increasing the number of detected particles, hence there is no increased shot noise [68, 69, 70, 71, 72, 73].

The field of quantum metrology allows sub-shot noise measurements by exploiting quantum properties of light, such as entanglement or squeezing [74]. Fundamentally, the measurement precision is limited by the number of probe particles N. While within the standard quantum limit (SQL), the relative standard deviation of the measured quantity σ scales with $\sigma = 1/\sqrt{N}$, one can, in principle, approach the Heisenberg limit $\sigma = 1/N$ with entangled states or squeezed light [73]. This has been experimentally verified in scanning microscopy configurations with entangled N00N states [75, 76] and squeezed light [77]. Moreover, full-field absorption imaging was demonstrated using entangled photons [78]. Unfortunately, all mentioned approaches only led to a modest improvement in the signal-to-noise ratio (SNR), mainly because of difficulties in producing the required states and high photon losses when working with entangled states[8] [74].

While it is commonly known that one can surpass the SQL with entangled states or squeezing, it was only recently brought into focus that multiple interactions of a probe particle with the sample can also approach the single-pass Heisenberg limit without the need of preparing highly delicate quantum states [70, 71, 72, 73]. With this approach, several experimental successes were achieved: A phase estimation with a variance of more than 10 dB below the SQL [73], a 1700-fold signal enhancement (compared to diffraction-limited microscopy) with a high-finesse scanning microcavity [80], and a contrast enhancement in full-field double-pass transmission microscopy [81].

In 2016, the scheme was adapted to full-field multi-pass microscopy by placing the sample in a self-imaging cavity, which allows capturing an image with enhanced contrast by re-imaging a pulse of light onto the sample multiple times [68]. This multi-passing technique has been applied to absorption and polarization microscopy [68]. Furthermore, it was used for phase microscopy [82] and the creation of high orbital angular momentum states [83]. It was also suggested to apply the multi-passing scheme to electron microscopy [84].

[8] However, there are several proposed schemes for further optimizing the use of entangled photons for quantum metrology. See for example [79].

1.5. Goal and structure of the thesis

While multi-pass microscopy was already used to image biological cells in absorption microscopy [68], the goal of our approach is to combine interferometric imaging with multi-pass microscopy to further increase the detection sensitivity of small nanoparticles and thus to enable dynamic studies of even smaller proteins. This could lead to advances in the understanding of microscopic processes, ultimately even to numerous applications in molecular biology and biomedical research. For example, a dynamic observation of small proteins could contribute to plasma protein binding studies, which play a critical role in the drug development process [85, 86, 87], or the identification of biomarkers of various diseases such as cancer [26, 88].

Hence, we have developed an interferometric multi-pass microscope, which allowed us to demonstrate that interferometric multi-pass imaging of 100 nm gold nanoparticles obtains better sensitivity compared to single-pass imaging as a proof-of-concept experiment. In chapter 2, I elaborate on some basic imaging theory and the working principle of iSCAT and multi-pass microscopy. Moreover, I introduce the boundary element method (BEM) simulations that we used to validate our experimental results and predict the optical response of proteins, which our group wants to observe in the future.

In chapter 3, the microscope development process is outlined, which includes considerations about the illumination and detection scheme, our choice of optical and optomechanical components, and designing the setup within the 3D CAD software SolidWorks. Next, I report on the assembly of the microscope in the laboratory and discuss several issues we encountered while making our first observations. Then, the results of our initial tests of the multi-passing scheme are presented. As a next step, experimental observations of gold nanoparticles and a validation with the BEM simulation are shown. Moreover, I also describe the implemented background subtraction scheme and the acquisition of a defocus curve, which allowed us to properly compare our experimental data of gold nanoparticles with the simulation. Furthermore, I present the results of the above-mentioned proof-of-concept experiment, where we showed that interferometric multi-pass imaging of 100 nm gold nanoparticles obtains better sensitivity compared to single-pass imaging. Finally, a noise analysis of the setup, BEM simulations of further nanoparticles, and potential setup improvements, including simulations of a new imaging scheme, are presented. Note, that I am continuously changing between explaining what we did, why we did it, and presenting results in chapter 3 so that the reader can follow a coherent storyline of our microscope development process.

In chapter 4, all findings are reviewed, and strategies to further optimize or redesign the setup are discussed. This should lead the way for future interferometric multi-pass imaging of single proteins.

As it is tradition in the field, I have come up with an acronym for our new imaging technique and would like to call it multi-pass interferometric scattering microscopy (MP-iSCAT).

2. Theory

2.1. Phase-contrast microscopy

If a sample in a microscope is illuminated with coherent monochromatic light, according to Abbe's imaging theory [89], the intensity at the detector I_{det} can be written as the interference between scattered and unscattered (or reference) light:

$$I_{det}(x, y, z) \propto |\overline{E}_r + \overline{E}_s|^2 = I_r + I_s + 2\, E_r\, E_s \cos\varphi \tag{1}$$

where $\overline{E}_r = E_r\, \mathrm{e}^{\mathrm{i}\,\varphi_r}$ and $\overline{E}_s = E_s\, \mathrm{e}^{\mathrm{i}\,\varphi_s}$ are the complex electric fields of the reference and scattered light, respectively (with E_r and E_s as their real amplitudes). Spatial dependencies and vectorial notation are omitted for easier readability. The three resulting terms are contributions of the reference field ($I_r = |\overline{E}_r|^2$), the pure scattered light ($I_s = |\overline{E}_s|^2$) and the interference term ($2\, E_r\, E_s \cos\varphi$) where $\varphi = \varphi_r - \varphi_s$. In Zernike's phase-contrast microscopy [7], a $\frac{\pi}{2}$ phase mask is introduced into the path of the reference light, as depicted in figure 1.

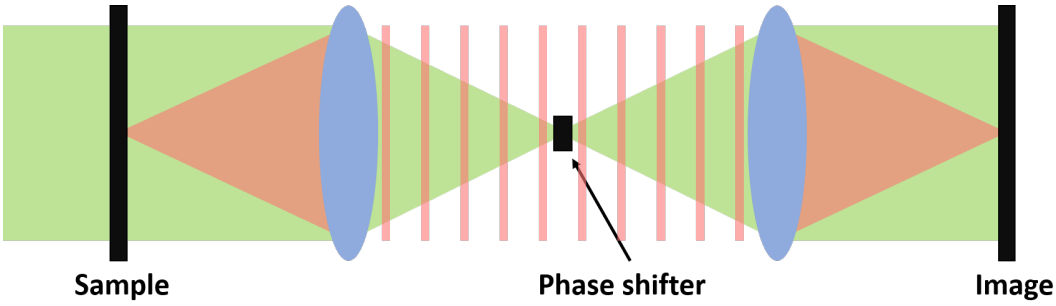

Figure 1: Zernike phase-contrast microscopy in a 4f setup with an on-axis phase mask. The unscattered (=reference) light is shown in green and the scattered light in red.

Hence, the reference light is focused down after the first lens and gets phase-shifted by $\frac{\pi}{2}$ when passing through the phase mask. As a result of the focusing, the reference light acquires an additional Gouy phase shift[9] equal to π. Thus, the effective phase change of the reference light is $\frac{3\pi}{2}$ (compared to a fictitious plane wave that propagates from the object plane to the image plane without the 4f system) [93].

The scattered light from a sample with a real refractive index, i.e. the sample is non-absorptive, emerges from the object with the same phase as the illumination light. It only obtains a partial $\frac{\pi}{2}$ Gouy phase shift upon being focused onto the image plane in the far-field. Therefore, unscattered and scattered light are fully out of phase and interfere depending on φ, which generates image contrast [93].

[9] This phase shift was first observed by Gouy [90], and intuitive explanations of its physical origin can be found in [91, 92].

2.2. iSCAT

2.2.1. Imaging theory

Abbe's imaging theory is so universal, that equation (1) can also be used to describe several other imaging schemes, including bright-field, dark-field, and interferometric microscopy [24]. To describe bright-field imaging[10], one only has to replace the reference field $\overline{E}_r$ with an illumination field $\overline{E}_i$. The optical extinction, i.e. shadow of the object, is then described by the cross-term in equation (1) and can be thought of as the sum of absorption and scattering [24, 94]. In dark-field microscopy, the reference light is blocked, and the only remaining contributing term in equation (1) is the scattered intensity I_s. In contrast, when working with interferometric imaging, I_s can be neglected as the interferometric cross-term ($2\,E_r\,E_s\cos\varphi$) is orders of magnitude larger than the pure scattering term.

When focusing on the detection of particles which are smaller than the wavelength of the illuminating light, the optical response of the particle (modeled as a spheroid with semi-axes $a_{1/2/3}$) can be formulated as $\overline{E}_s \propto \alpha \overline{E}_r$ where

$$\alpha_i = \epsilon_0\, V \left(\frac{\epsilon_s - \epsilon_m}{\epsilon_m + L_i(\epsilon_s - \epsilon_m)} \right) \tag{2}$$

denotes the polarizability of the particle along the semi-axis a_i [24, 95]. V is the volume of the particle, L_i the depolarization factor along a_i. For a sphere, $a_1 = a_2 = a_3$ and $L_i = 1/3$. The parameters ϵ_s and ϵ_m are the dielectric functions of the scatterer and the embedding medium respectively and ϵ_0 is the dielectric constant. For metals, such as gold or silver, the denominator of equation (2) can reach a minimum, hence enhancing their scattering response. However, for commonly used metallic nanoparticles, the scattering response is only enhanced by one order of magnitude when using visible light. Thus, the main contributing factor for scattering is the particle volume V. As a consequence, the scattering field $\overline{E}_s$ scales with the third power of the particle size, and the scattering intensity ($I_s = |\overline{E}_s|^2$) scales with the sixth power of the particle size [24, 96].

This scaling behavior explains why I_s, which scales quadratically with the scattered field, becomes much weaker compared to the cross-term in equation (1), which scales linearly with the scattered field, when observing small nanoparticles. Therefore, interferometric detection of small nanoparticles is superior compared to dark-field detection on the grounds of a different scaling behavior of the different terms in equation (1), since the experimental implementation of ultrasensitive dark-field microscopy faces challenges because small nanoparticles only scatter a limited number of photons which are challenging to detect and differentiate from background noise [24, 96].

Besides the experimental challenges in dark-field detection, there is also an experimental

[10] No phase-mask is used in bright-field imaging.

advantage of working with an interferometric imaging scheme: Interferometric detection overcomes some sources of noise (dark current and read noise in the camera and contributions of incoherent stray light), which can be thought of as a result of a homodyne detection between scattered and reference light. By choosing an appropriate reference light intensity, this advantage can even be extended to the point where the detection is only limited by the shot noise of the signal [38, 48]. A more detailed analysis of different noise sources in interferometric imaging is outlined in section 2.2.3.

The iSCAT signal of interest, i.e. the interferometric cross-term, can be obtained by subtracting the reference intensity I_r, which acts as a background, from the measured intensity (and neglecting the scattering term I_s): $I_{det} - I_r \approx 2\,E_r\,E_s\cos\varphi$. Thus, the image contrast C when comparing images with and without a nanoparticle, can be formulated as

$$C \approx \frac{2\,E_r\,E_s\cos\varphi}{I_r} = 2\,\frac{E_s}{E_r}\cos\varphi \tag{3}$$

This result might lead to the illusion that a better sensitivity, i.e. the ability to detect smaller iSCAT signals, can be reached by simply minimizing E_r in the denominator. However, the resulting increased contrast is at the expense of the overall signal, which leaves the signal-to-noise ratio constant in shot noise-limited detection, as long as $E_r \gg E_s$ [24, 39, 96].

The phase angle φ between reference and scattered light in iSCAT imaging is a strong function of the focus position of the microscope objective. This dependence can be understood when realizing that the path length of the reference and scattered light cannot be altered independently. More precisely, a particle, illuminated with a monochromatic incident plane wave along the optical axis (i.e. polar angle $\theta = 0°$), scatters most light to larger polar angles θ, while the reference light only travels into one direction: either forwards or backwards the optical axis, depending on the imaging geometry. Thus, the scattered and reference light propagate (mostly) along paths with different θ, which results in a change of the phase angle when altering the focus position of the microscope. In this sense, interferometric imaging schemes can be seen as a common-path homodyne interferometer, in which the phase angle between the reference and the scattered light can be altered by changing the focus position of the objective [48, 97]. Unfortunately, the strong dependence of the iSCAT contrast on the phase angle φ can severely complicate finding the right focus position and thus identifying weak scatterers as they are often only revealed in image post-processing [39].

2.2.2. Resolution limit

Even though there are several ways to define a resolution limit in microscopy (mostly depending on the use of coherent or incoherent light) [98], Abbe's resolution limit [99]

$$R = \frac{\lambda}{2\,NA} \tag{4}$$

is a suitable approximation. Here, R denotes the lateral resolution limit, λ is the wavelength of the illumination light, and NA is the numerical aperture of the system. For a derivation of Abbe's resolution limit, see, for example, [100]. Although the resolution limit prevents us from distinguishing structures that are smaller than half the wavelength of the illuminating light, I want to emphasize that iSCAT can still be used to observe smaller objects without resolving them, i.e. one only sees a diffraction-limited spot. As the contrast in equation (3) depends on the volume of the particle, it is even possible to differentiate between nanoparticles of different sizes and masses [27, 31, 38, 48].

2.2.3. Imaging noise

All experimental measurements in the real world are limited due to the presence of certain random and non-random signal fluctuations, which are called noise. In the case of iSCAT, this noise can originate from various different sources. Even though iSCAT employs a common-path geometry, mechanical vibrations of the various optical components can lead to image noise as these mechanical vibrations can translate to non-compensable path-length variations of the scattered and reference light. It is especially unfavorable if different components vibrate differently with respect to each other. Thus, iSCAT microscopes are typically set up on vibration-isolated optical tables. Moreover, using stable optomechanical components, mounting critical components like the objective on heavy stages, securely fastening all components, and covering the setup to shield it from air movements during the experiment, is vital for the detection of single proteins [101, 22].

A second type of noise is stray light and camera-read noise. Stray light can originate from outside the microscope (from ambient light, for example), but mainly comes from reflections and scatterings from optical components that are part of the microscope. These internal reflections and scatterings can usually be reduced by decreasing the illumination intensity. Camera-read noise can be attributed to thermal noise in the chip of the camera and its associated amplifier electronics. Modern cameras can have reasonably low levels of noise, and as the iSCAT signal is typically a small intensity variation on top of a high background, camera read noise is usually not a major concern [24, 97].

However, the camera-read noise sets a lower boundary for the operating range, the so-called 'dynamic range', of a camera. The upper bound is given by detector nonlinearities and saturation effects. To convert the analog camera signal into a digital signal, an appropriate bit depth is chosen, based on the dynamic range [24]. For our camera, this is 12 bit, which imposes a limit on detecting small signals in a single frame[11] by setting the read-out resolution to 1 in 4096, i.e. $2 \cdot 10^{-4}$.

Another noise source is the surface roughness of the used coverslips. Tiny surface inhomogeneities lead to a refractive index that differs from the surrounding medium, which causes

[11] And under normal operating settings.

unwanted scattering. Already a nanometer roughness leads to a non-random contrast noise of 0.3 % in reflection iSCAT [25] and 0.5-1 % in SP-IRIS setups [97] and thus sets a limit on nanoparticle detection [102]. However, this non-random noise appears as a static background, i.e. it is reproducible in consecutive acquisitions. Therefore, it can be removed with background subtraction schemes, which are further outlined in section 2.2.4.

Finally, laser power fluctuations and beam pointing instabilities are often the most prominent noise sources in iSCAT experiments [39, 96]. While experimental measures, such as sending the illumination laser beam through a single-mode fiber or avoiding any moving parts in the vicinity of the laser, can improve the situation, it is usually inevitable to account for laser intensity fluctuations via referencing or normalization when trying to detect iSCAT contrasts smaller than 10^{-3} [96]. In confocal imaging, a balanced photodiode pair can be used to reach a stability in the order of 10^{-7} if a point detector is used [103, 104]. In wide-field detection, referencing can be similarly implemented by comparing the total power recorded within each frame. As the scattered field and the reference field both share the same laser noise and ultimately both contribute to the iSCAT contrast, they naturally self-reference [24].

Even if one manages to cope with laser power fluctuations, one is still confronted with the fundamental probabilistic arrival of photons at the detector and its associated noise, the so-called 'shot noise' [24, 96]. Discrete probabilistic events, like the arrival of photons at a detector, behave according to the Poisson distribution [67]. Thus, the standard deviation for the fluctuations of the photon number in one image acquisition, i.e. the shot noise, is given by

$$\sigma_1 = \sqrt{N} \tag{5}$$

where 1 indicates one acquisition and N is the mean photon number per acquisition[12]. If we now calculate the relative standard deviation σ_{rel}, we get

$$\sigma_{1,rel} = \frac{\sigma_1}{N} = \frac{1}{\sqrt{N}} \tag{6}$$

Thus we see that the relative contribution of shot noise decreases if the number of collected photons is increased. The interferometric signal in equation (1) is given by $2\,E_r\,E_s\cos\varphi$ and since $E_s \propto E_r$, the signal is proportional to N. Due to the Poissonian statistics, the shot noise is proportional to $\sqrt{N}$. Thus, the associated signal-to-noise ratio (SNR) scales with

$$SNR \propto \frac{N}{\sqrt{N}} = \sqrt{N} \tag{7}$$

As a consequence, we can conclude that the image quality can be improved, and thus making it possible to detect smaller iSCAT contrasts, by simply collecting more light if the limiting factor in an experiment is shot noise. However, experimentally the amount of de-

[12] This can be a single pixel or a whole frame.

tectable photons is still limited by the dynamic range of the detector. Fortunately, there are ways to overcome this limitation with certain image analysis methods. A demonstration of the effect of shot noise on nanoparticle detectability in iSCAT imaging is shown in figure 2.

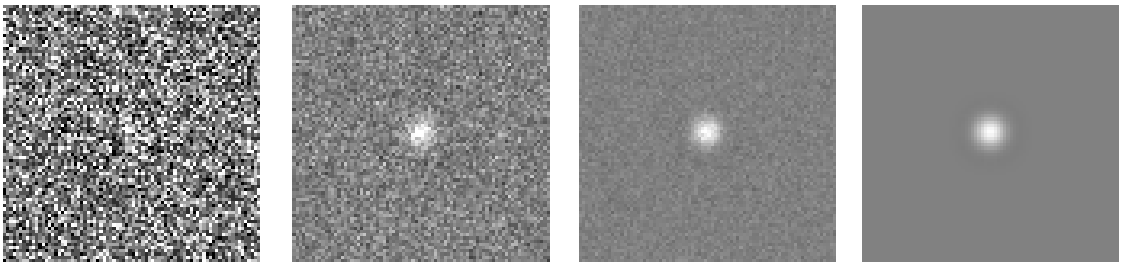

Figure 2: Demonstration of the effect of shot noise on nanoparticle detectability in iSCAT imaging. On the very right, an artificially-made signal of a nanoparticle is shown in the absence of shot noise. In the three remaining images, shot noise was simulated with a shot noise generator by Erez Posner [105]. From left to right, the full well capacity in the simulation was changed by a factor of 10 from one image to the next.

2.2.4. Image analysis

As outlined in the previous chapter, the ability to detect smaller iSCAT signals, i.e. the sensitivity, can be improved by collecting more photons if the defining noise source is shot noise[13]. There are two different approaches to collect more photons. On the one hand, one can simply increase the illumination intensity. However, one has to make sure that the camera is not saturated, which sets an upper limit on the reference intensity. To counteract this issue, one can implement an attenuator in the detection path of the reference light [38, 39, 49, 64]. This can also make it easier to find the optimal focus position if the cover glass roughness becomes visible in a single acquired image, i.e. without the need for averaging frames [39].

On the other hand, image analysis methods, which are widely used in the field [25, 26, 59, 64], can be employed to increase the effective photon number after the actual experiment. For this, one can either average over multiple frames (temporal binning) or sum up adjacent pixels (spatial binning). Naturally, temporal binning trades temporal resolution, and spatial binning decreases the image resolution. In most cases, temporal binning is of particular interest because it is nowadays technically possible to average over several hundreds or even thousands of frames in a reasonable timeframe if the setup is stable[14] during the averaging time. To examine how the relative shot noise scales when averaging over n frames, we calculate the relative standard deviation for n frames

$$\sigma_{n,rel} = \frac{\sigma_n}{n \cdot N} = \frac{\sqrt{n \cdot N}}{n \cdot N} = \frac{1}{\sqrt{n \cdot N}} = \frac{\sigma_{1,rel}}{\sqrt{n}} \tag{8}$$

[13] Reminder: Shot noise is fundamentally always the remaining noise source, and even experimentally, it is often the final significant remaining noise [25, 26, 53, 55, 62].

[14] With respect to mechanical vibrations, temperature drifts and laser fluctuations.

and see that it scales proportionally to the relative shot noise of a single frame and decreases as more frames are acquired. Qualitatively, this means that acquiring more frames should lead to an improvement in image contrast, similar to how it is shown from left to right in figure 2. Obviously, in real life, one cannot capture an infinite number of frames and reproduce an image quality as it is depicted on the very right in figure 2.

Other powerful image analysis methods for iSCAT are background removal and dynamic imaging. As already outlined, the surface roughness of the coverslip can lead to background signals that limit the detection of nanoparticles. However, as these features are static, they can be removed by subtracting a background image from the actual image. For dynamic events, like the arrival of a protein on a coverslip, this can be done particularly successfully. For particle tracking, it is usually not even necessary to record a separate background image as an average image can serve as a background [102].

Even though the fundamental principle of dynamic imaging is simple, different variations of the method can be used for different applications, mainly depending on the possible image acquisition speed and the speed at which the nanoparticle moves [96]. For example, subtraction of a temporal average [106] or a rolling-window average across stacks of frames can be employed [27]. For particle tracking applications, an advanced iterative-estimation algorithm can be found in [107]. Valuable suggestions on how to use image processing for binding studies are outlined in [39]. If other noise sources are suppressed, and dynamic imaging is used, shot noise-limited imaging can be achieved experimentally [25, 26, 53, 55, 62].

2.2.5. Illumination schemes

There are two different approaches for illuminating a sample in an iSCAT setup, confocal and wide-field illumination. In a confocal configuration, a laser beam gets focused onto the sample plane and is rapidly scanned over the sample. In state-of-the-art iSCAT microscopes, the scanning is usually done with acousto-optic deflectors[15] (AODs) [25], which can provide scanning speeds of up to hundreds of MHz. If confocal illumination is used, one has to ensure that the beam scanning is finished within the exposure time of the camera.

In wide-field illumination, the whole field of view is illuminated simultaneously with an extended beam of light. Naturally, the acquisition speed in confocal imaging is limited by the speed of the AODs. Additionally, the sample experiences a higher peak laser power due to the focusing of the illumination light onto the sample. While wide-field illumination does not need expensive AODs for rapid scanning, the illumination light is focused inside the objective, which can give rise to unwanted stray light and, in a worst-case scenario, even damage the objective if sufficient illumination power is used.

However, in most applications, it is still beneficial to move the illumination light beam in wide-field illumination so that the sample is illuminated from different angles [108]. If the

[15] Sometimes these devices are called acousto-optic modulators (AOMs), which are essentially the same.

movement is performed within the exposure time of the camera, this leads to an averaging of signals originating from unwanted scatterers, like dust on optical components, while the nanoparticle of interest remains in focus. This wide-field illumination scheme can be implemented by placing two galvanic mirrors[16] in a conjugate image plane before the sample and sweeping the illumination light beam [108], as depicted in figure 3.

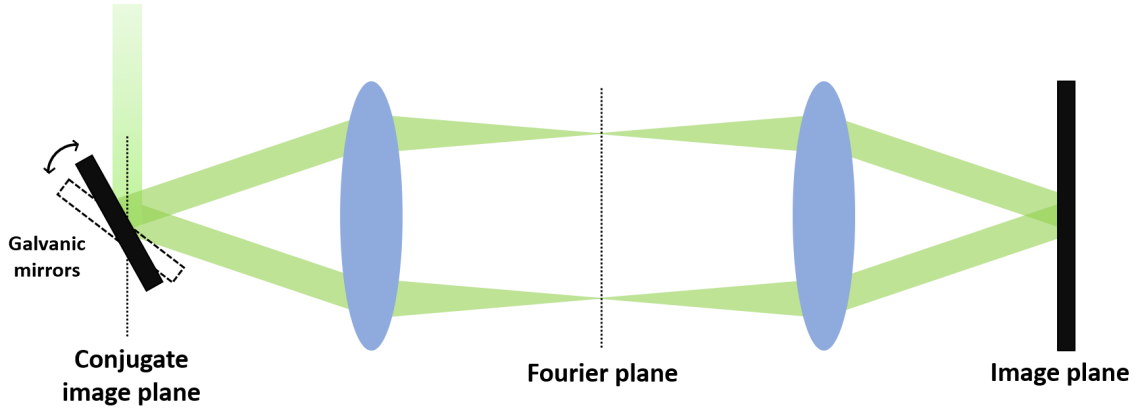

Figure 3: 2D representation of the wide-field illumination scheme with galvanic mirrors to illuminate the sample from different angles. The resulting image averages over unwanted scatterers on optical components as the components are illuminated on different positions during the acquisition time. If two galvanic mirrors are placed close to each other in the illumination beam path, a circular motion of the beam in the Fourier plane can be achieved with two sinusoidal input signals.

If the microscope is operated with wide-field illumination and a rotating sample illumination scheme, it is essential to restrict the NA of the illumination light, because high-NA illumination light usually only contributes to the reference light in small nanoparticle imaging, which ultimately decreases the iSCAT contrast according to equation (3). Even if a high-NA illumination ray hits the sample and scatters, the scattered light propagates outside the possible collection range of the objective with a higher probability [39, 49]. This can be intuitively understood when considering that the induced dipoles from a high-NA ray are orientated in a more vertical position than for a low-NA ray. The more vertical orientated dipoles from the high-NA rays emit scattered radiation preferred to directions which are (close to) orthogonal to their dipole axes. Thus, a large part of the scattered light propagates outside the collection range of the objective.

As a consequence, the above-mentioned wide-field illumination scheme with galvanic mirrors has to be restricted to small sweeping angles. The exact restriction depends on experimental conditions, including the sample of interest, NA of the used objective, and general imaging scheme (reflection iSCAT, COBRI or SP-IRIS).

Another interesting consideration is that iSCAT does not necessarily require coherent (laser) illumination if operated in a wide-field illumination scheme. Other light sources can

[16] A galvanic mirror is basically a mirror that is moved with an electric motor. They are significantly cheaper than AODs but not as fast and precise.

be used as long as the coherence length of the light is sufficiently large, i.e. the path length difference between the scattered and reference field is smaller than the coherence length of the illumination light [48, 96]. As previously mentioned, partially-coherent LEDs are used as illumination sources by the SP-IRIS community [48, 54].

Finally, several focus position stabilization schemes have been incorporated into iSCAT setups [25, 26]. Usually, the common idea is to reflect a separate laser beam somewhere on the sample stage and monitor the motion of the reflected beam. The sample stage is then moved accordingly to counterbalance any unwanted movements or drifts of the sample stage.

2.2.6. Summary

Comparing dark-field microscopy with iSCAT leads to the conclusion that iSCAT is better suited for the detection of small nanoparticles because of a superior scaling behavior of the particle size in equation (1), as it is experimentally easier to detect a small intensity variation on top of a large background, as it is done in iSCAT, compared to detecting a very small absolute signal, like it is done in dark-field microscopy.

The cover glass roughness is a noise source that can severely limit nanoparticle detectability, but it can be overcome with background subtraction or dynamic imaging. After the image subtraction, nanoparticle detection can already be shot-noise limited [25], and contrast-detection can already be as low as 10^{-3} [26]. To further improve the sensitivity, one can further increase the number of detected photons. This is usually achieved with averaging over multiple frames (temporal binning), which requires a stable setup during the acquisition time. If one manages to average over several thousand frames (while keeping the setup stable), a contrast-detection in the order of 10^{-4} has been achieved experimentally [26].

An additional improvement can be reached by attenuating the reference light. The attenuation is vital if the microscope is operated in transmission mode to not saturate the camera. If the reference light is attenuated, the illumination intensity can be increased, which leads to more scattered light at the camera and thus gives a better contrast according to equation (3). The increased contrast by the use of an attenuator lowers the need for long temporal binning [39], which is especially beneficial if the setup cannot be held stable over extended periods of time or a higher acquisition rate is needed. Furthermore, an increased scattering contrast can also make it easier to find the optimal focus position if the cover glass roughness becomes visible without the need for averaging any frames [39].

Finally, if a wide-field illumination scheme is used, it is beneficial to average over the signal from unwanted scatterers by illuminating the sample from different angles within the exposure time of the camera. Nevertheless, one has to restrict the illumination NA to not decrease the iSCAT contrast excessively.

2.3. Multi-pass microscopy

If a microscopy technique is limited by shot noise, multi-pass microscopy can be used to improve the obtained signal without increasing the associated shot noise [68, 69]. When combining iSCAT with multi-pass microscopy, this can be intuitively understood by realizing that the re-imaging of a pulse of light onto the sample leads to an increased amount of scattered light and hence improves the contrast according to equation (3). As the detection of the light only takes place after multiple rounds of re-imaging, shot noise is only generated once, when the light is detected.

As already outlined in the introduction, multi-pass microscopy is a quantum optimal way to amplify a signal, which means that its SNR-improvement scaling is the same as for other quantum metrology schemes [68, 69]. Thus, multi-passing can overcome the shot-noise limited scaling of $\sigma_{1,rel} = \frac{1}{\sqrt{N}}$ and approach the theoretical Heisenberg limit $\sigma_{1,rel} = \frac{1}{N}$ which is a fundamental limit set by quantum mechanics [70, 71, 72, 73]. Furthermore, multi-pass microscopy currently seems to be easier to implement than imaging schemes with entangled or squeezed photons because of difficulties in producing the delicate entangled or squeezed photon states [74].

Within the discipline of multi-pass microscopy, one can distinguish between three different operating schemes, namely continuous wave (CW), ring-down (RD), and multi-passing (MP). In the CW scheme, a continuous beam of light is in- and outcoupled into the self-imaging cavity, which generates a power build-up inside the cavity. In the RD scheme, a pulse of light is incoupled into the cavity, and a fraction of it is outcoupled every time the pulse interacts with one of the semi-transparent end mirrors of the cavity. The detection can then be in a time-resolved way, in which the number of interactions is recorded, or by integrating over the outcoupled light. The MP scheme operates similarly to the RD scheme, but the pulse of light interacts with the sample for a specific number of times before it is outcoupled and detected [69].

While the best signal improvement can be achieved within the CW scheme, it is more challenging to experimentally implement as the cavity has to be stabilized so that it is resonant. Even though the MP scheme gives a slightly better improvement than RD in recent theoretical considerations and simulations [69], the RD mode is often chosen for an experimental implementation because it is more challenging to implement a mechanism to outcouple all light at once after a specific number of roundtrips[17] in a MP scheme.

So far, a RD scheme with temporal postselection by a gated CCD camera [68] and with a Pockels cell with polarizing beam splitter [109] have been experimentally implemented. In principle, it would also be possible to position the Pockels cell and the polarizing beam splitter as an optical switch inside the cavity to outcouple all light at once [68]. However, this approach is experimentally more difficult as the Pockels cell and the polarizing beam splitter

[17] One roundtrip usually is in a time range of some nanoseconds.

introduce losses inside the cavity, which become more severe with every additional roundtrip. Moreover, a very precise alignment of the two components would be necessary to re-image the light onto the same sample position in every roundtrip.

As outlined in section 2.2.1, the phase angle φ between the reference and the scattered light in iSCAT can be changed by slightly altering the focus position of the microscope. This feature can typically be used to set the optimal phase angle in a way so that the contrast is maximized by slightly defocusing the microscope if necessary. However, in our proposed combination of iSCAT and multi-pass microscopy, the sample has to remain exactly in focus as a precise re-imaging of the sample would not be possible with an introduced defocus. Thus, the reference light should be phase-shifted by $\frac{\pi}{2}$, similar to how it is done in phase-contrast microscopy [7].

2.4. Boundary element method (BEM) simulations

To validate our experimental findings and be able to predict the iSCAT contrast of future experiments in our setup, we have used the metallic nanoparticle boundary element method (MNPBEM) toolbox [110], which is implemented in MATLAB. To simulate our setup with the toolbox, we have adapted publicly available code [111] from the SP-IRIS community, which was used for simulations in [48] and [97]. Our code can be found in [112].

At the core, the MNPBEM toolbox uses the boundary element method (BEM) [113] to calculate the surface charges of a nanoparticle, which result from an incoming light wave. These surface charges are then used as the basis for the optical response of the nanoparticle[18]. Within the BEM, Maxwell's equations get simplified to surface integrals at the nanoparticle-medium interface. In this way, one only needs to mesh the surfaces and calculate the surface integrals at the interfaces, which is faster than volume-based approaches [48].

Our simulations are structured as follows: First, we specify the imaging geometry, including the direction, polarization, and wavelength of the incoming light, which is modeled as a monochromatic plane wave. Moreover, the size and shape of the nanoparticle get specified, as well as the refractive index of the nanoparticle and the surrounding media. The toolbox then calculates the surface charges at the nanoparticle-medium interface as a response to the incident plane wave. From there, it furthermore calculates the scattered far-fields in the angular spectrum representation.

The imaging concepts from section 2.1 can equivalently be described with the angular spectrum representation. Within this formalism, the light field gets decomposed into plane waves (and evanescent waves) with variable amplitudes and propagation directions. One can now ask how the light field $\vec{E}(\vec{r}) = \vec{E}(x, y, z)$ looks like at an arbitrary z-plane[19] if one has

[18] The MNPBEM toolbox can - despite its characteristic name - also be used to simulate the optical response of non-metallic nanoparticles, see [48], for example.

[19] As commonly used in the literature, z is the direction of propagation.

knowledge about the field at the plane $z = 0$. The answer[20] is given by the angular spectrum representation [114]:

$$\vec{E}(\vec{r}) = \iint_{-\infty}^{\infty} \hat{\vec{E}}(k_x, k_y, 0)\, \mathrm{e}^{\,\mathrm{i}\,[k_x \cdot x + k_y \cdot y \pm k_z \cdot z]}\, \mathrm{d}k_x\, \mathrm{d}k_y \tag{9}$$

where $\hat{\vec{E}}$ is the 2D Fourier transform of $\vec{E}$, k_x and k_y are the spatial frequencies (or reciprocal coordinates), and $k_z = \sqrt{k^2 - k_x^2 - k_y^2}$ with the wave vector $k = \frac{2\pi n}{\lambda}$ and refractive index n. The $\pm$ sign in the exponent makes sure that both, the wave propagation into the half-space $z > 0$ ($+$ sign) and $z < 0$ ($-$ sign), are included.

Coming back to the simulation, the toolbox calculates the scattered far-field in the angular spectrum representation $\vec{E}_\infty(k_x, k_y)$, expressed as the complex-valued magnitudes of plane wave components. To form an image of the scattered light in the far-field, we evaluate the canonical angular spectrum integral[21] over the microscope's collection angle θ_{max} with appropriate prefactors [48, 114]:

$$\vec{E}_{scat}(\vec{r}) = \frac{\mathrm{i}}{2\pi} \iint_{\theta \le \theta_{max}} \vec{E}_\infty(k_x, k_y)\, \mathrm{e}^{\,\mathrm{i}\,[k_x \cdot x + k_y \cdot y + k_z \cdot z]}\, \frac{1}{k_z}\, \mathrm{d}k_x\, \mathrm{d}k_y \tag{10}$$

where the integration limit makes sure to correctly simulate that we are only collecting those plane wave components that are allowed by the NA of our microscope objective.

To simulate an interferometric image, we also have to implement the reference light field $\vec{E}_{ref}(\vec{r})$, which was modeled as a simple plane wave whose phase and amplitude could be changed.

To simulate the final intensity image $I(\vec{r})$ at the camera, we coherently add the scattered and reference light field

$$I(\vec{r}) = |\vec{E}_{ref}(\vec{r}) + \vec{E}_{scat}(\vec{r})|^2 \tag{11}$$

and ultimately calculate the normalized intensity

$$I_{norm}(\vec{r}) = \frac{I(\vec{r})}{I_{ref}(\vec{r})} \tag{12}$$

where $I_{ref}(\vec{r}) = |\vec{E}_{ref}(\vec{r})|^2$. Expressed as a normalized intensity, it is possible to compare the outcome of our simulations with the contrast of equation (3). Note that our BEM simulations did not include any multi-passing. A successful multi-pass operation of the final setup should lead to an even larger nanoparticle contrast compared to the results of our simulations.

[20] Under the assumption of a homogeneous, isotropic, linear, and source-free propagation medium.
[21] The canonical angular spectrum integral can be derived from equation (9), for details see [114].

3. Methods and Results

3.1. Microscope development

The development process of our interferometric multi-pass microscope was driven by two key principles: Minimizing photon loss inside the self-imaging cavity and designing the setup in a way so that the sample can be placed onto a horizontally oriented microscopy cover glass. In this section, first, an overview of the entire planned setup, including the illumination and detection scheme, is given in section 3.1.1. Next, the choice of optical and optomechanical components for the multi-pass setup of our microscope is outlined in sections 3.1.2 and 3.1.3. Then, the development of the multi-pass setup with the 3D CAD software SolidWorks, which included designing custom-made adapters and a proper assembly of all components, is presented in section 3.1.4. Finally, considerations about the galvanic mirror system for a rotating sample illumination, as outlined in section 2.2.5, and about the development of an attenuator ring, whose benefits are explained in sections 2.2.1 and 2.2.6, will be presented in sections 3.1.5 and 3.1.6.

After outlining the microscope development process, our conducted experiments, as described in section 1.5, are presented in sections 3.2 to 3.5.

3.1.1. Illumination and detection scheme

We decided to set up our interferometric multi-pass microscope in transmission mode and use wide-field illumination. The decision for using a transmission configuration is naturally given by the imaging scheme of multi-pass microscopy because a large portion of the illumination light is reflected at the incoupling end mirror, which would complicate the detection in reflection mode. Combining a confocal illumination with the multi-passing scheme would also overcomplicate the detection. A schematic of the full setup is shown in figure 4.

Starting with the illumination path, a pulsed Monaco 1035 (40 W) from Coherent is frequency-doubled and sent through a pair of lenses to get an appropriate beam diameter. Additionally, a half-wave plate and a polarizing beam splitter (PBS) give the possibility of continuously changing the illumination light intensity.

Next, the beam impinges on two galvanic mirrors (Pangolin ScannerMAX Compact 506), which are driven by a two-channel function generator (RIGOL DG900). As the galvanic mirrors are placed in an image plane, it is possible to illuminate the sample from different directions, as outlined in section 2.2.5. Further details about the galvanic mirror system can be found in section 3.1.5.

Before the illumination light enters the self-imaging cavity, a beam splitter (BS) can outcouple back-reflected light from the multi-pass setup to the alignment tool, which consists of one camera in an image plane and one camera in a Fourier plane. Both cameras are

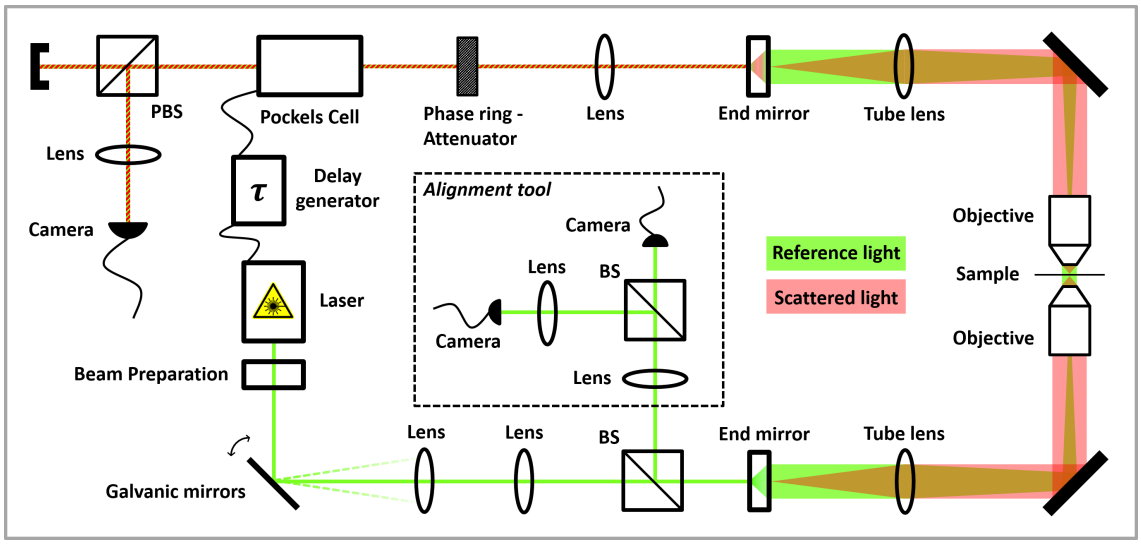

Figure 4: Schematic of the whole interferometric multi-pass microscope, including the illumination and detection path.

BLACKFLY S from the company FLIR. As the name already reveals, the alignment tool supports the alignment process of the multi-pass setup. For this, component after component get introduced into the imaging path, and their position and orientation are changed until the beam impinges at the same position (and with the same beam diameter) on the two alignment cameras as before the component got placed into the imaging path.

Coming to the multi-pass setup, the illumination light gets incoupled via the lower end mirror and illuminates the sample in a wide-field configuration after passing through the lower tube lens and objective. At the sample, some light scatters (shown in red) and is collected by the upper objective. It then forms an image at the upper end mirror, and the majority of scattered and unscattered light (reference light, shown in green) gets re-imaged onto the sample.

At the upper end mirror, a fraction of the scattered and unscattered light is outcoupled at every roundtrip. It then passes through the attenuator in a Fourier plane. Details about the attenuator are presented in section 3.1.6. With the following Pockels cell (KD*P EM520-TT-HHT-AR517 from Leysop) and the polarizing beam splitter, one can look at individual passes or sum up multiple passes (ring-down mode). To precisely control the timing, we use a delay generator (DG645 from Stanford Research Systems), which first triggers a laser pulse and, after an adaptable delay time, triggers the driver of the Pockels cell. If the Pockels cell is triggered, the polarization of the light is changed, so that it gets reflected towards the camera at the polarizing beam splitter. As light is naturally propagating with the speed of light, one roundtrip inside the self-imaging cavity only takes around 5.2 ns. Thus, it is essential that the delay generator and the Pockels cell can operate faster than that, which is ensured by a sub-nanosecond time resolution of the delay generator and a combined rise and fall time of the Pockels cell of around 2 ns. The pulse length of our laser is significantly shorter than

the roundtrip time, which ensures that no power-buildup is happening inside the self-imaging cavity.

For capturing the interferometric image, we use a CMOS camera (MV1-D1024E-160-CL) from Photonfocus, which offers a high dynamic range, high SNR, high acquisition speeds (150 fps[22] at the full resolution of 1024x1024), and is also used by other iSCAT groups [25, 101]. In order to handle the high data flow from the camera, we use a Bitflow Neon-CLD frame grabber. The frame grabber and the camera are controlled with self-written MATLAB code. By implementing two lenses with different focal lengths in the detection path, an additional magnification of the image can be introduced if needed.

3.1.2. Choice of optical components

As the working principle of a multi-pass microscope is the re-imaging of photons onto the sample multiple times, we had to ensure that as few photons as possible get lost in the imaging process. Thus, choosing optical components with very high transmission or reflection was important. The choice of our illumination wavelength (517.5 nm) was predetermined by the shared laser[23] in the lab.

The most critical choice of an optical component in our multi-pass setup was the objective as it determines the amount of scattered light we can collect, specified by its numerical aperture (NA), and is prone to have a lower transmission compared to single-lens elements as modern objectives are made out of multiple lenses to correct for image aberrations. Thus, we discarded the use of immersion objectives due to their significantly lower transmission rates compared to air objectives.

We decided to use Zeiss Plan-Apochromat 20x/0.8 objectives as their specifications include a very high transmission at our illumination wavelength (around 99 %[24]). Moreover, they include optical corrections for image aberrations, offer a decent NA of 0.8, and were significantly more affordable compared to custom-made solutions. As Zeiss objectives need a compatible tube lens in order to accurately correct for some image aberrations, we combined our objectives with suitable Zeiss tube lenses for which we measured a transmission of over 99 %.

As end mirrors of the self-imaging cavity, we chose high energy partially reflecting laser mirrors (CVI PR1-532-xx-1025 where xx is the reflectance in percent) from the company CVI Laser Optics. A 90 % reflectance mirror (in-coupling) and a 95 % mirror (out-coupling) were used in the setup.

In order to be able to observe biological samples on a horizontally oriented microscopy cover glass, we designed a part of the microscope in a vertical orientation. Hence, we set up half of the components on an optical breadboard, which was located above our optical table.

[22] The acquisition speed can be significantly improved if a smaller region of interest is defined.
[23] More details about the laser and the illumination scheme are outlined in section 3.1.1.
[24] In the lab, we measured a transmission of 98 %.

To guide the imaging path through the vertical section, we implemented two $45°$ Nd:YAG laser line mirrors from Thorlabs (NB1-K12), which have a reflectance of over 99.8 % at our illumination wavelength.

3.1.3. Choice of optomechanical components

Setting up half of the microscope onto an optical breadboard made the overall setup sensitive to mechanical vibrations, which could decrease the image contrast. Hence, the optomechanical components and the breadboard itself were chosen with the main focus on mechanical stability. Another design criterion was to implement the multi-pass setup in a modular structure so that it can easily be adapted or upgraded. The modules include two end mirror modules, two tube lens modules, and a lower and upper objective module. All stages (that are part of the modules) were chosen to be able to translate in x, y, and z and have a tip/tilt capability for the alignment process.

For the end mirror and tube lens modules, 3-axis MicroBlock stages (MBT616D/M) from Thorlabs were used as they are a reasonable compromise between mechanical stability and affordability. To add a tip/tilt capability, precision kinematic mirror mounts (KS1T) from Thorlabs were mounted onto the MicroBlock stages. Connecting the stages and the mirror mounts in a stable and adaptable way required us to design custom-made adapters, which is outlined in the next section.

For the objective modules, we chose 3-axis NanoMax stages with closed-loop piezos (MAX311D/M) from Thorlabs as they give us the ability to control the focus very precisely with the included piezos. A 3-channel piezo controller (BPC303) from Thorlabs was used to control the piezos. To further increase the stability of the objectives and be able to control the tip/tilt angles precisely, we decided to mount the objectives onto gimbal mirror mounts (GM100/M) from Thorlabs. For connecting the gimbal mounts to the NanoMax stages, we again designed custom-made adapters.

As sample holder, we decided to use an xy translation mount (XYF1/M) from Thorlabs, which was planned to be mounted on the bottom side of the optical breadboard, but was discarded due to stability issues. Instead, the lower objective module was redesigned and a new sample holder (a mirror mount for two-inch optics, MXI-2-3027, from Radiant Dyes) was mounted to the lower piezo NanoMax stage, which was previously used for the lower objective module. The translation stage of the lower objective module was changed to an xy steel extended contact translation stage (TSD-1202SH-M6) from SIGMA KOKI, which gave the lower objective a fixed z-position as the new sample stage was now able to translate in z by being mounted onto the piezo NanoMax stage. Illustrations of the old and new sample holder (including the whole setup) are shown in the next section in figure 5 and 7.

For an increased stability of the whole setup, we used a custom-made solid aluminium breadboard (1200x600 mm) with a thickness of 20 mm from Radiant Dyes. The increased

thickness (compared to standard optical breadboards) makes the board stiffer so that any mechanical vibrations that are present on the optical table translate to similar vibrations (in amplitude and frequency) on the breadboard. The breadboard includes a custom cut-out for the vertical part of our microscope. To securely mount the breadboard onto the optical table, we used five 1.5 inch thick stainless steel posts.

3.1.4. 3D CAD Design

As a next step, the whole multi-pass setup was visualized within the 3D CAD software 'SolidWorks'. 'SolidWorks'-files of the Thorlabs stages and optomechanical components were imported, and custom-made adapters, needed for connecting the stages with the mounts of the optical components, were designed with the software. We designed the adapters so that the position of the mounted optical components can be changed over a wide range. Moreover, we focused on the mechanical stability of the connections between the adapters and the stages and making the connections suitable for a simple alignment process.

Thus, the adapters were designed so that they could slide on the top plates of the stages over a wide range while having the possibility to secure them with four screws in (almost) all positions. Additionally, all adapters include a small extrusion, which is orientated orthogonal to the imaging path, to give the opportunity to orientate the mirror mounts, and thus also the optical components, with a close-to-optimal yaw angle in the initial alignment process. To be able to position the upper objective close enough to the sample, we replaced the standard top plate of the NanoMax stage of the upper objective with a right-angle top plate (AMA011/M from Thorlabs) and mounted the adapter of the gimbal mount onto the side of the stage. After the design process, the custom-made adapters were manufactured by the workshop of our faculty.

Next, the 'SolidWorks' assembly of the whole setup was thoroughly checked for compatibility errors, especially if the optical components can be positioned so that the distances between them are correct and adaptable. Appropriate revisions of the setup and the adapters were done in multiple cycles. Figures of the final modules and the associated adapters can be found in the appendix A.1.

The final complete multi-pass assembly is shown in figure 5, and an image of the corresponding setup in the laboratory can be found in figure 6.

To isolate the microscope from ambient light, air movements, and to dampen acoustic noise, we designed a box that can be placed over the setup. We used the 25 mm optical construction rail system from Thorlabs together with plastic-coated cardboard panels with foam core (TB4 from Thorlabs) for the sides of the box and black cardboard (TB5 from Thorlabs) for the top[25]. A SolidWorks assembly of the the whole multi-pass setup together with the box can be found in the appendix A.2.

[25]We used TB5 for the top because the standard size of TB4 was too small.

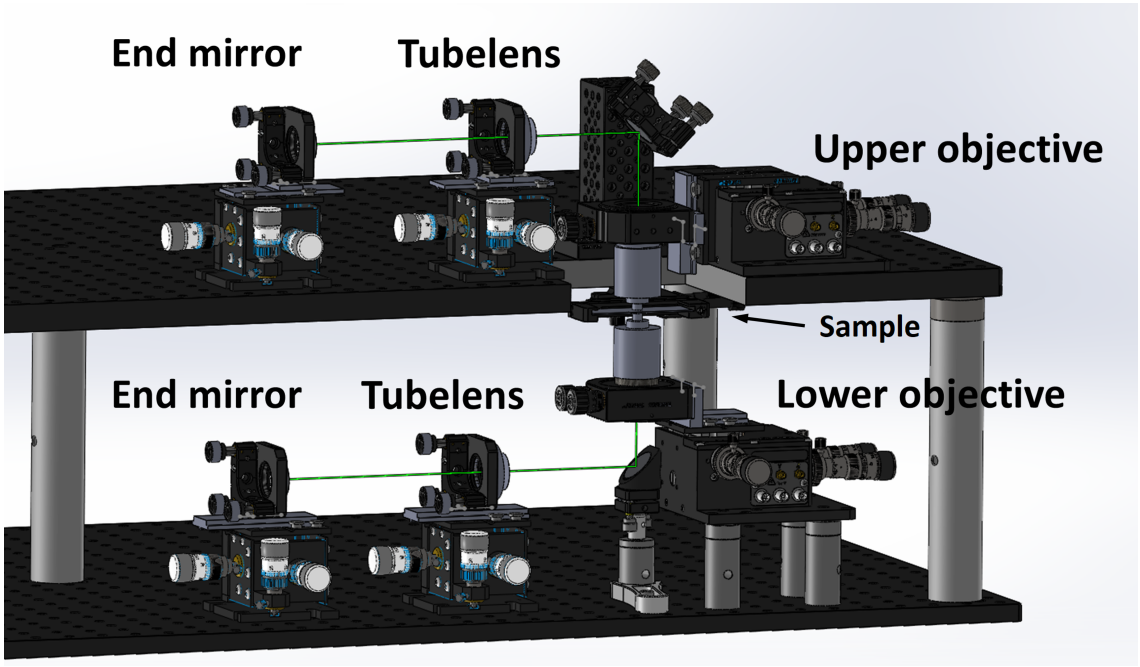

Figure 5: Assembly of the complete multi-pass setup including the optical breadboard, the sample holder, all modules, and the two $45°$ mirrors. The imaging path is highlighted in green.

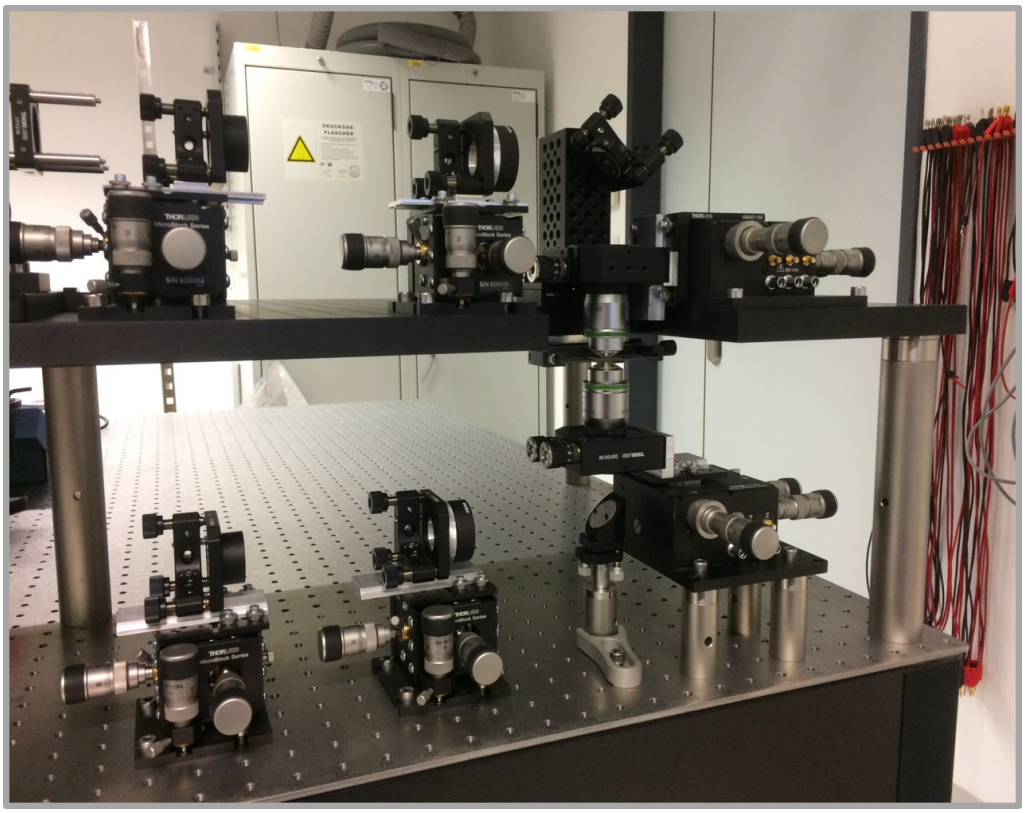

Figure 6: Corresponding multi-pass setup in the laboratory.

As outlined in section 3.1.3, the initially selected sample holder was discarded due to stability issues. Instead, the lower objective module was redesigned and a new sample holder was mounted to the lower piezo NanoMax stage, which was previously used for the lower objective module. The setup with the modified sample holder and lower objective module can be seen in figure 7.

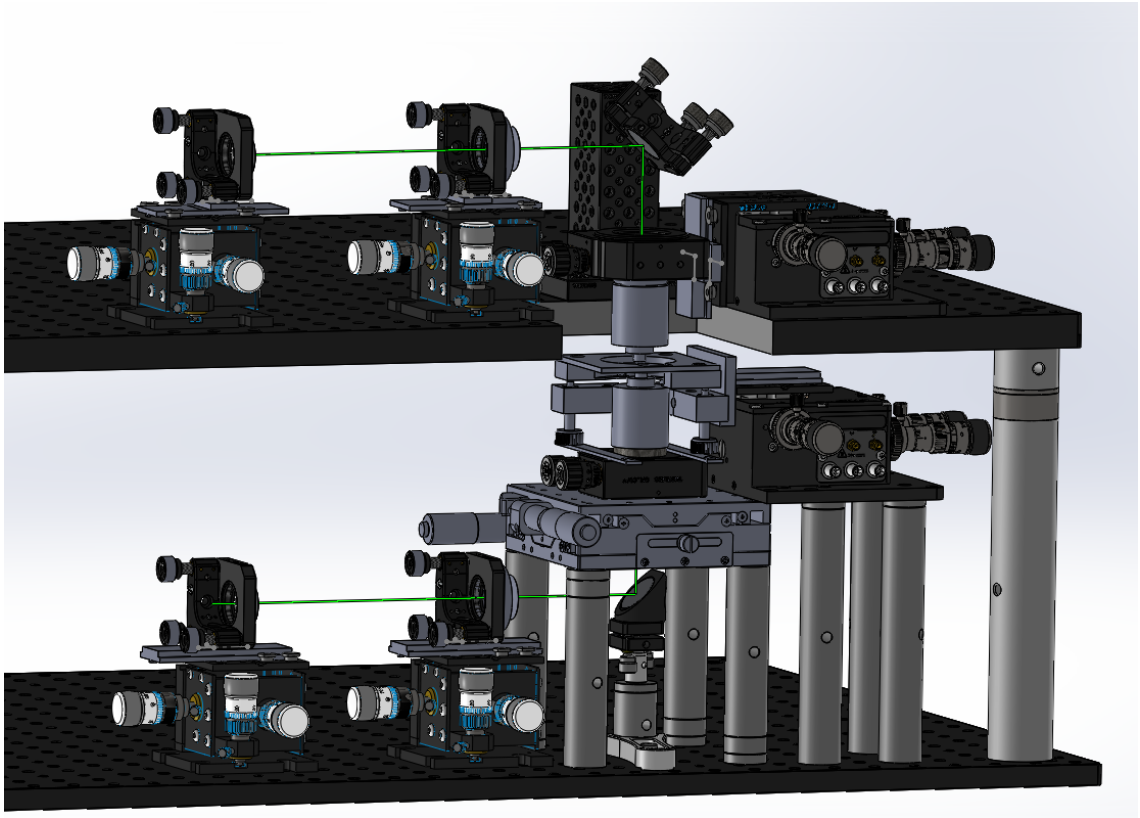

Figure 7: Setup with modified sample holder and lower objective module. In this setup, the z-position of the lower objective is fixed while the sample can translate in z. The imaging path is shown in green.

3.1.5. Galvanic mirror

To choose a suitable galvanic mirror system, we focused on two specifications: scanning speed and mirror size, while also monitoring the price and availability of the system. For the scanning speed, we wanted to be able to move the galvanic mirrors with a sinusoidal signal, and thus getting a circular motion in the Fourier plane, so that at least one loop in an exposure time of 10 ms (at the needed deflection angle) is possible[26]. The needed deflection angle was calculated with an ABCD matrix approach [115] to be around $3°$, where the main deflection limitation was the back aperture of the objective.

On the one hand, the galvanic mirrors' diameter should be as small as possible because

[26] These speeds are easily achievable with galvanic mirrors, which are significantly cheaper than AODs.

that allows a faster mirror motion[27]. On the other hand, the mirrors should be large enough so that no light is hitting the edge of the mirrors, which could introduce stray light into our microscope.

Thus, we first reduced the beam diameter with two lenses before it hits the galvanic mirrors. For this, we tried to make the beam as small as possible to exclude as many unwanted scatterers as possible while still illuminating a field of view (at the sample) of around 20 micrometers (diameter). Therefore, we decided to reduce the given beam diameter from 4.0 mm ($1/e^2$) to 1.3 mm. As it is not guaranteed that we will always be able to hit the galvanic mirrors perfectly in the middle, we decided that a mirror size of 5 mm would be desirable.

Finally, we decided to implement the ScannerMAX Compact 506 galvanic mirror system (with MACH-DSP digital servo driver and UP150D power supply) from Pangolin Laser Systems as they provided the highest speed[28] in their price category and could be assembled with 5 mm mirrors.

3.1.6. Attenuator

At a Fourier plane in the detection path, the scattered light is spread out over the whole collection NA while the reference light is focused down to a point. Thus, a dot attenuator can be placed in the focus position of the reference light, which attenuates the reference light while most of the scattered light can propagate unaffectedly. To be able to combine an attenuator with our rotating illumination scheme, as outlined in section 2.2.5, we had to design the attenuator in the shape of a ring that can be placed in a Fourier plane in the detection path. Additionally, as mentioned in section 2.3, our attenuator ring should also introduce a $\frac{\pi}{2}$ phase shift to the reference light.

In order to lose as little scattered light as possible at the attenuator ring, we decided to mount the window on which the attenuator will be placed in a tilted position at the Brewster angle. Thus, the scattered light, which is mostly p-polarized in our setup[29], cannot be reflected by the window.

We decided to employ a transmission rate of the attenuator of around 10^{-4}, which is similar to the attenuation approach of other interferometric microscopes in transmission mode [38]. In reflection iSCAT and SP-IRIS, the used attenuators are more transmissive[30], simply because only a portion of the illumination light is reflected in their schemes and serves as reference light [38, 39, 49].

[27] The scanning speed of galvanic mirrors is mainly limited by the generated heat. A larger mirror size translates into a larger load for the motors, which results in more heating.

[28] The Compact 506 galvanic mirrors can be driven at 1800 Hz at a deflection angle of 4° (verified in our setup). This gives us around 18 loops in 10 ms, which is well above our set criterion.

[29] We use p-polarized illumination light and assume that the scattering process does not significantly change the light's polarization.

[30] Reflection iSCAT used an attenuator with a transmission rate of around $1 \cdot 10^{-2}$ [38, 39] and SP-IRIS with $5 \cdot 10^{-2}$ [49].

To find out which diameter the attenuator ring should be, which depends on the deflection angle of the illumination beam, we first had to decide which illumination angle we want to use. As outlined in section 2.2.5, the illumination NA has to be restricted to not decrease the iSCAT contrast excessively. Thus, we experimentally checked how far we could increase the deflection angle at the galvanic mirrors until the contrast got noticeably worse. The associated experiment, which resulted in a maximum illumination NA of 0.3, is presented in section 3.2. This translates to a ring diameter of 4 mm at the Fourier plane in the detection path.

We wanted to choose the thickness of the attenuator ring in the transverse direction such that only a portion of the light that is one order of magnitude smaller than the planned transmission rate of 10^{-4} can propagate outside the ring. Therefore, we simulated a 2D Gaussian distribution of the form

$$f(x, y) = \mathrm{e}^{-\frac{2(x^2+y^2)}{\sigma^2}} \tag{13}$$

where the minimum waist $\sigma = \frac{2\lambda f}{\pi w_0}$ after the focusing through a lens was calculated with the measured beam diameter of $w_0 = 1.3$ mm $(1/\mathrm{e}^2)$ [115]. Then we checked which ring thickness would only leave 10^{-5} of the light unattenuated and found it to be 164 micrometers. As our calculations were done with a theoretical minimum beam diameter, we decided to choose a transverse attenuator ring thickness of 0.5 mm. Thus, the attenuator ring should be implemented at a radius position of 1.75 - 2.25 mm on the Brewster window. If the attenuator ring is mounted in a tilted position as outlined above, the effective ring size will decrease, but as we increased the transverse ring thickness from the calculated 164 micrometers to 0.5 mm, we should still attenuate enough reference light. Additionally, we also decided to order a dot attenuator to be able to operate the microscope without any rotating sample illumination or with only tiny deflection angles and chose a diameter of 2 mm for the attenuation disk.

Last but not least, we had to choose which materials and thicknesses to deposit on the Brewster window to get our desired attenuation and phase shift. We decided to use aluminium for the attenuation together with a layer of BaF_2, which protects the metal layer and co-determines the phase shift, because both materials can easily be deposited on top of a glass window and the layer thicknesses can be precisely controlled.

The right thicknesses of the aluminium and BaF_2 layers for our desired attenuation and phase shift can be calculated with the Fresnel equations. We decided to use a transfer-matrix method Python package by Steven J. Byrnes [116] and cross-check its results with the Luxpop thin film calculator by Guillaume Boisset [117], which are both optimized tools for calculating the Fresnel equations in a stack of thin films. Refractive indices of $n_{\mathrm{BaF2}} = 1.48$ and $n_{\mathrm{Al}} = 0.85{+}6\mathrm{i}$, obtained at our illumination wavelength from [118], resulted in a thickness of 280 nm (BaF_2) and 60 nm (Al) for a phase shift of $\frac{\pi}{2}$ and a transmission rate of $1.5 \cdot 10^{-4}$.

As a last note, all presented experiments in the following are done without an attenuator because the manufactured pieces only arrived after the experiments were conducted.

3.2. First observations

For our first experimental tests, we operated our microscope without multi-passing and a rotating sample illumination. Thus, we removed the upper end mirror and introduced another half-wave plate into the setup, so that the polarization could be set such that all light in the detection path gets reflected towards the camera at the polarizing beam splitter. First, we introduced the half-wave plate into the detection path before the Pockels cell. Consequently, the small half-inch aperture of the half-wave plate decreased the NA in the detection path, which, according to equation (4), decreased the resolution of our microscope as can be seen in figure 8.

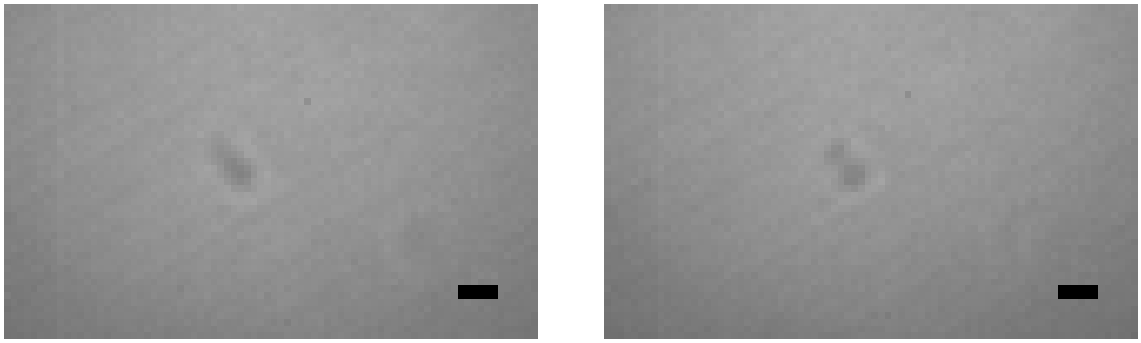

Figure 8: Dust or dirt particle with (left) and without (right) half-wave plate in the detection path. The half-inch aperture of the half-wave plate limits the detection NA which manifests in a decreased resolution in the left image. Scale bars: 0.95 µm.

Therefore, we placed the half-wave plate into the illumination path before the galvanic mirrors so that the detection NA is not decreased. There were, however, two other imaging artifacts, which can be seen in figure 8. First, a vertical stripe, close to the left edge of the two images, and second, diagonal stripes (from the lower left corner to the upper right corner) in the background are visible. Both phenomenons did not change their shape or orientation when changing the illumination angle or rotating the camera. However, the diagonal stripes were only reproducible when using our illumination wavelength. As a consequence, the chip of our camera was exchanged, which removed the vertical stripe, but the diagonal stripes are still visible when using an illumination wavelength of 517.5 nm.

Thus, we concluded that the diagonal stripes are probably an interference effect which is intrinsic to the camera chip design and our illumination wavelength. To get rid of the diagonal stripes in the background, one could use another illumination wavelength, but this would have required us to change all optical components, which are optimized for 517.5 nm, and employ another light source, or one could consider to use another camera. However, as the stripes are a static feature, they should be removable with a background subtraction scheme, similar as described for the signal originating from the cover glass roughness in section 2.2.4.

Next, we started our rotating illumination scheme with the galvanic mirrors and checked how far we could increase the deflection angle until the contrast got noticeably worse. For

this, we applied two $\frac{\pi}{2}$ phase-shifted sinusoidal input signals with a frequency of 200 Hz to the galvanic mirrors and again focused the microscope onto some dust or dirt particle between two cover glasses. After increasing the amplitude of both sinusoidal input signals, we re-focused the microscope manually by moving the upper objective in the z-direction. Three images with different illumination angles and corresponding decreasing contrast can be seen in figure 9.

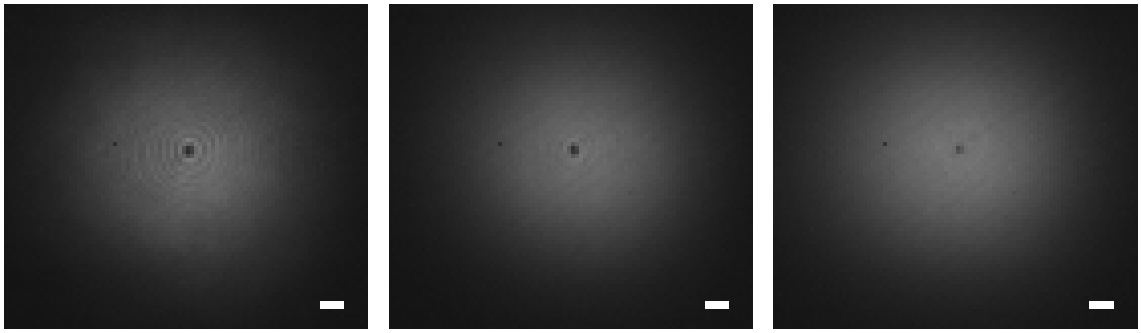

Figure 9: Left: Dust or dirt particle without rotating sample illumination. Middle: With rotating sample illumination corresponding to an illumination NA of 0.11. Right: With rotating sample illumination corresponding to an illumination NA of 0.32. The camera exposure time was set to 60 ms. Scale bars: 3.18 µm.

We think that the decreasing contrast with higher illumination angles is a result of the mechanism described in chapter 2.2.5, in which a higher NA illumination leads to scattered light that is propagating outside the possible collection angle of the objective with higher probabilities, which forces us to restrict the illumination NA in order not to decrease the nanoparticle contrast excessively. Thus, we decided to use a maximum illumination NA of 0.3. Nevertheless, one can see in figure 9 that the rotating illumination scheme leads to a smoother background as intended, which is a result of averaging over different illumination angles. This effect should make it easier to only detect nanoparticles in the sample plane as signals from unwanted scatterers, like dust on optical components, get diminished by averaging over different illumination angles.

Finally, we checked if the rotating illumination scheme at an NA of 0.3 really gives a circular beam movement with a diameter of around 4 mm in the Fourier plane in the detection path for the planned attenuator ring. Our measurement could roughly replicate the 4 mm diameter, and we decided that a more precise measurement was not necessary, as the amplitude of the galvanic mirror motion can be changed continuously, and a fine-tuning of the amplitude to match the attenuator ring size has to be performed with the attenuator ring. Moreover, the beam spot size in the Fourier plane of the attenuator also seemed to be in the same order of magnitude as our calculations.

3.3. Multi-pass demonstration

To test if the multi-passing scheme of our setup is working as intended, we imaged a dummy water sample between two anti-reflection coated cover glasses and collected a MP-trace, which is our terminology for recording the intensity in a region of interest at the camera while sweeping the delay time between the laser pulse and the Pockels cell trigger in 0.1 ns steps. The repetition rate of the laser was set to 1 kHz, and the laser and the Pockels cell driver were externally triggered by the delay generator. Note that the zero position of the delay time in the following plots is arbitrarily set before the first pass. The first MP-trace was collected while ordinary protected silver mirrors were used as $45°$ mirrors for guiding the imaging path through the vertical part of our setup. The trace is shown in figure 10.

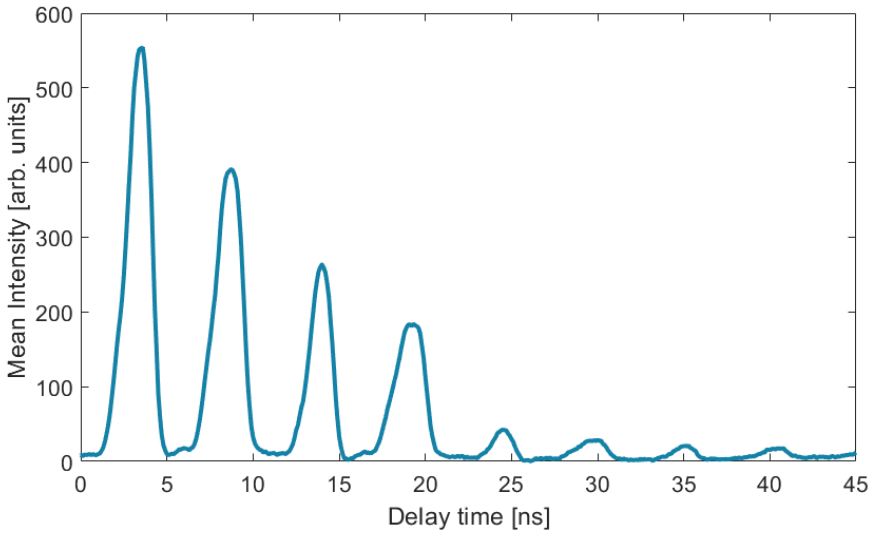

Figure 10: MP-trace with ordinary protected silver mirrors as $45°$ mirrors in the setup.

One can see that the intensity from the first to the second peak (which correspond to the first and third pass[31]) is decreased by around 30 %. After the seventh pass, there is hardly any light left inside the self-imaging cavity.

The next MP-trace was recorded with two Nd:YAG laser line mirrors (Thorlabs NB1-K12) as $45°$ mirrors. The trace can be seen in figure 11.

Here, the intensity drop between the first few passes is only around 14 %. Considering that 6 % of the light intrinsically gets lost at the two end mirrors (which have a reflectivity of 99 % and 95 %) in each roundtrip, we lose around 8 % of the light in each roundtrip inside the self-imaging cavity which includes any misalignment and absorption, unwanted reflections, and scattering at all optical components inside the cavity and at the sample.

[31] The second peak corresponds to the third pass as we are only collecting light that leaves the self-imaging cavity at the upper end mirror. Thus, the second peak occurs after one full roundtrip of the re-imaged light and consequently has already passed the sample three times. The following peak corresponds to the fifth pass and so on.

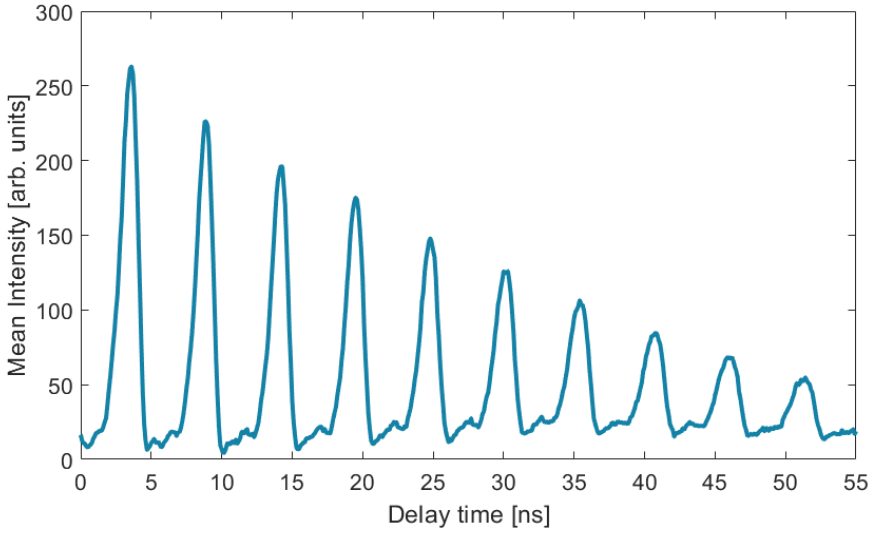

Figure 11: MP-trace with Nd:YAG laser line mirrors as $45°$ mirrors in the setup.

Thus, we concluded that the multi-passing scheme works as intended with a loss of around 8 % per roundtrip, which enables us to capture a pulse of light that has interacted with the sample 19 times (last intensity peak in figure 11).

3.4. Nanoparticle detection

3.4.1. Gold nanoparticles and comparison with BEM simulations

As a next step, we imaged 100 nm gold nanoparticles to further test if we are able to observe interferometric signals of small nanoparticles in our setup. Furthermore, we decided to use our BEM simulations to validate if we are successfully imaging 100 nm gold nanoparticles, as distinguishing dust or dirt on the cover glasses from the gold nanoparticles proved to be difficult. We used 100 nm diameter gold nanoparticles from Sigma-Aldrich (in citrate buffer) and diluted them with distilled water in a ratio of 1:100. We chose gold nanoparticles as a test sample because they are an affordable and reliable test sample which is widely used in the field.

Before pipetting the diluted nanoparticles between two cover glasses, we properly cleaned each cover glass right before using it. For this, we rinsed them multiple times with distilled water and isopropanol. Next, the remaining isopropanol was wiped off with a lens cleaning tissue (MC-5 from Thorlabs). After that, we cleaned both sides with a lens cleaning tissue and a drop of methanol. The microscope was again operated without multi-passing or the use of an attenuator, but a rotating sample illumination (illumination NA of 0.11 and repetition rate of 500 Hz) was employed. The camera exposure time was set to 40 ms. An image of a suspected 100 nm gold nanoparticle is shown in figure 12.

In order to be able to properly compare our experimental findings with the BEM simulation,

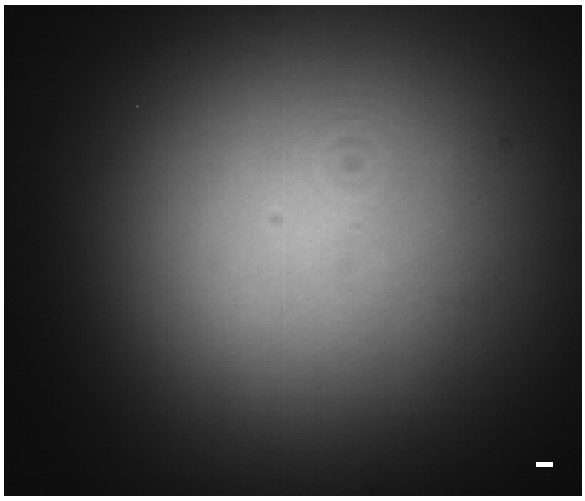

Figure 12: The suspected 100 nm gold nanoparticle is visible as a faint dark spot on the left to the vertical stripe in the middle of the picture. The bigger spot on the upper right side of the image is probably a dust particle that is located in an image plane as it is not averaged out by the rotating illumination scheme. Scale bar: 0.95 µm.

we performed the following steps. First, we acquired a background image with a flat-fielding scheme. For this, we slightly defocused the microscope so that the nanoparticle was not distinguishable from the background anymore and moved the sample stage, with the help of the piezos, in the transverse direction to nine different positions in a rectangular shape where the nearest positions were separated by 5 µm. At each position, an image was recorded, and a pixel-by-pixel average of these nine images served as our background image.

Next, we refocused onto the nanoparticle and moved the sample stage over a range of 10 µm in steps of 200 nm in the z-direction with the piezo. At each step, an image was recorded, which effectively gave us a defocus scan of the nanoparticle. The defocus scan gives a characteristic signal of the nanoparticle, which allows us to properly compare it to our simulations, similar to how it was done in [48, 49]. Furthermore, an automated defocus scan is beneficial because finding the correct focus position manually can be tedious and error-prone. Moreover, for certain nanoparticle sizes and imaging geometries, there can be multiple focus positions where the contrast is maximized [119].

After recording the 50 images at different z-positions, each image gets normalized by dividing each pixel value with the corresponding pixel value from the background image. Then, the nanoparticle signal of each of the 50 images gets fitted with a 2D Gaussian curve. The initial guess of the xy-position for the fit is specified manually. The fitted amplitudes of the 2D Gaussian curves are then plotted against the defocus position, which leaves us with an experimentally obtained defocus curve. The flat-fielding scheme, the defocus scan (including the movement of the piezos), and the image processing were all implemented in self-written MATLAB scripts. Three images of the defocus scan of the nanoparticle shown in figure 12, can be seen in figure 13.

For our BEM simulation, we set the refractive index of the surrounding medium to the

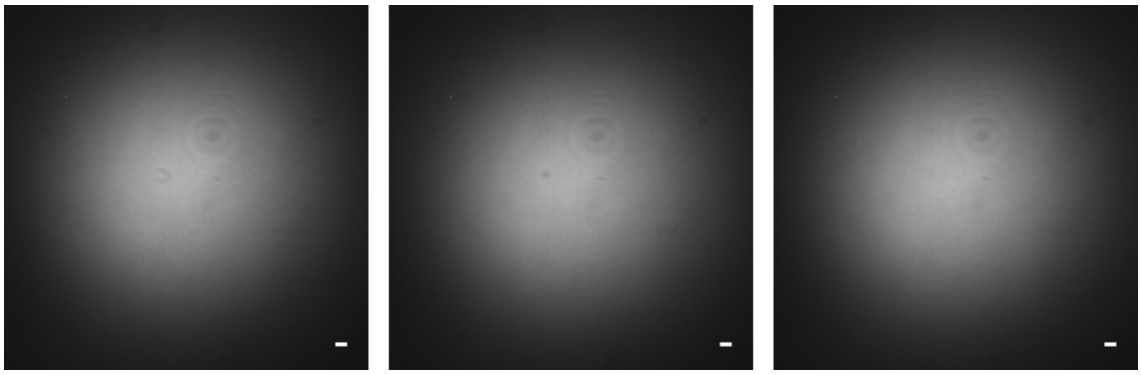

Figure 13: Three images of the defocus scan of the suspected 100 nm gold nanoparticle shown in figure 12, corresponding to defocus positions of -3 µm (left), -1 µm (middle), and $+2$ µm (right). Scale bars: 0.95 µm.

refractive index of water ($n = 1.33$) and placed the nanoparticle 2 nm above the cover glass ($n = 1.52$). The main calculations are then performed as outlined in section 2.4, but we added a simulation of the rotating sample illumination scheme by incoherently averaging over different illumination angles[32] with the actually used illumination NA of 0.11.

Finally, three experimentally obtained defocus curves and the simulated defocus curve are plotted together in figure 14. The BEM simulation code can be found in [112].

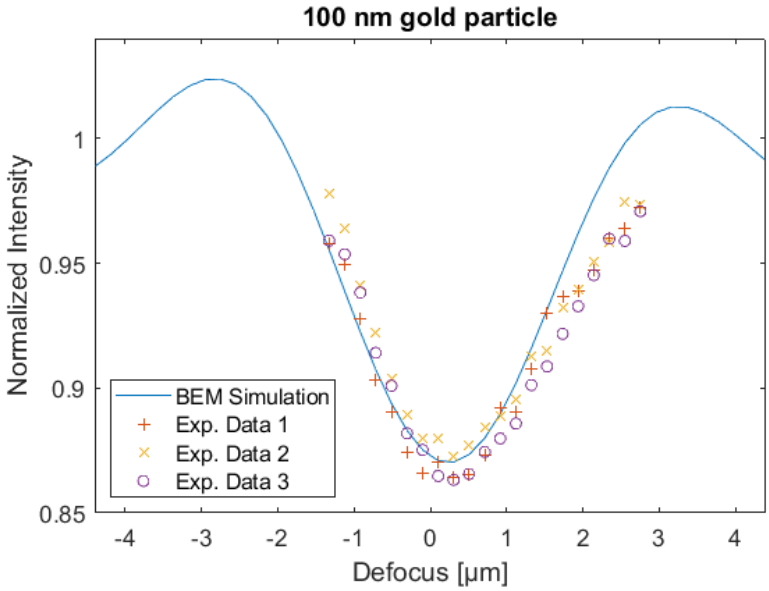

Figure 14: Comparison of experimentally obtained and simulated defocus curves of a 100 nm gold nanoparticle. The experimental defocus curves are obtained from the same nanoparticle, but the sample stage's xy-position was changed between the acquisitions.

The three experimentally obtained defocus curves in figure 14 are slightly manually shifted[33] in the x-direction of the plot so that the curves overlap with the simulation. This shift is justified since our experimental defocus scan gets started in the middle of the defocus range at

[32] For this comparison, we used 8 different equally-spaced illumination angles.
[33] All three curves are shifted for the same amount.

0 µm, but this middle position is set manually by only roughly focusing the microscope on the nanoparticle and thus has no claim to be at the real minimum of the defocus curve.

The reason why the experimentally obtained defocus curve is only plotted close to the focus position (and not for the whole defocus range), has to do with the 2D Gaussian fit that we used to determine the normalized intensity at a particular defocus position. As the normalized intensity values of the nanoparticle approach 1, and thus are hardly distinguishable from the background, the fit is not working reliably anymore. Moreover, a 2D Gaussian fit for values above 1 was not implemented. Thus, we excluded the defocus regions close to a normalized intensity of 1, as the main goal, i.e. validating that we are really imaging 100 nm gold nanoparticles, was already successfully accomplished.

As two interesting last notes, first, I want to mention that one can clearly see in figure 14 that the phase angle, which determines the contrast according to equation (3) in interferometric imaging, is a strong function of the focus position, as outlined in section 2.2.1. Second, as mentioned in [38], the normalized intensity in interferometric imaging can be above 1, which corresponds to a bright spot on a dark background (visible for example in the left image in figure 13), which conceptually shows that the acquired images in iSCAT are indeed interferometric images and not only simple shadow images.

3.4.2. Multi-pass detection of gold nanoparticles

After ensuring that we have the capability to successfully image 100 nm gold nanoparticles, we performed our proof-of-concept multi-pass experiment. For this, we again diluted 100 nm gold nanoparticles from Sigma-Aldrich with distilled water in a ratio of 1:100. The nanoparticles were pipetted between two anti-reflection coated cover glasses, and a rotating sample illumination (1 kHz at an illumination NA of 0.11) was used. The experiment was again performed without an attenuator. The repetition rate of the laser was set to 1 kHz, and we compared single-pass and multi-pass images by changing the delay time between the laser pulse and the Pockels cell trigger. The illumination intensity was held constant during the experiment. Images where a laser pulse interacted with the sample one, three, and five times are shown in figure 15.

It already looks like the contrast, i.e. the distinguishability from the background, is increased from the left to the middle image in figure 15. To validate this and quantify the improvement, the nanoparticle signal that is indicated with a red arrow in figure 15 got further analyzed. First, a mean of the background intensity in a region where no illumination light is hitting the camera (not shown in figure 15) was calculated and subtracted from the image, which effectively removed the camera dark current. Next, as the nanoparticle signal is a dark spot on a bright background, the minimum intensity value I_{min} of the nanoparticle was evaluated and divided by an average intensity value I_{mean} that was calculated in a region close to the signal but which did not include any nanoparticle signals. The nanoparticle contrast C

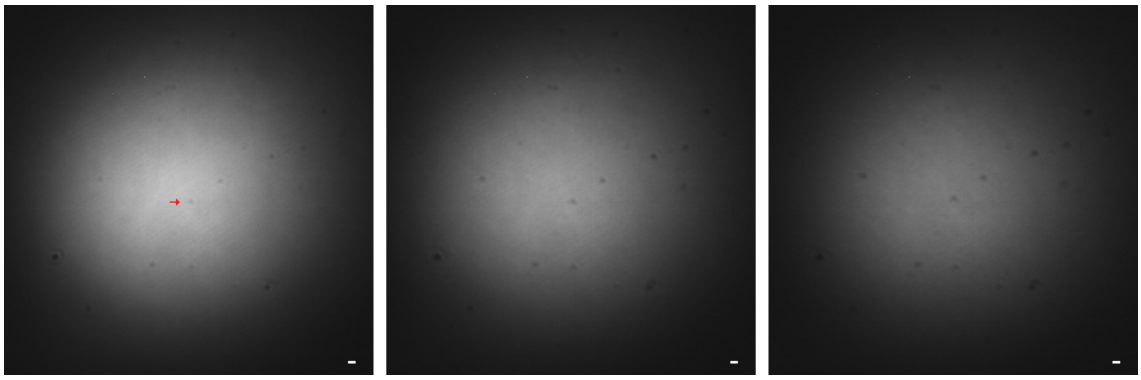

Figure 15: Multi-pass images of 100 nm gold nanoparticles. A pulse of light interacted one (left), three (middle), and five (right) times with the sample. The red arrow indicates which nanoparticle signal was further analyzed. Scale bars: 0.95 µm.

was then calculated with

$$C = 1 - \frac{I_{min}}{I_{mean}} \tag{14}$$

so that a higher contrast value corresponds to a better distinguishability from the background. This analysis was performed in the same way for all three images. It resulted in a contrast of 14.3 % for the single-pass image[34], 20.7 % for the image where the light interacted three times with the sample, and 20.3 % for the image where the light interacted five times with the sample. Hence, we concluded that our proof-of-principle experiment was successful in showing that an interferometric multi-pass image of our microscope can indeed obtain a better sensitivity compared to a single-pass image.

We think that the reason why the contrast slightly decreased from the three-pass to the five-pass image is mainly because of a suboptimal alignment of the multi-pass setup. Furthermore, when imaging gold nanoparticles with a diameter of 100 nm, the thin sample approximation, i.e. that the sample does only produce small phase shifts and that absorption can be neglected, is no longer valid.

3.4.3. BEM simulations of further nanoparticles

In preparation for future experiments, we decided to simulate the expected contrast of smaller gold nanoparticles and proteins in our setup with the BEM simulations, which are outlined in section 2.4. We planed to use smaller gold nanoparticles as further test samples to step-wise decrease the nanoparticle contrast and check if we can still detect the nanoparticles without the use of an attenuator. Thus, we simulated gold nanoparticles with diameters of 100 to 30 nm. We did not simulate a rotating sample illumination as the simulated contrast values with a rotating illumination scheme do not differ significantly, but the simulation time is increased

[34] A contrast of 14.3 % for the single-pass image is in good agreement with the expected contrast of a 100 nm gold nanoparticle as predicted by our BEM simulations in figure 14.

considerably. Furthermore, we did not simulate any attenuation or phase shift of the reference light. We again set the refractive index of the surrounding medium to the refractive index of water ($n = 1.33$) and placed the nanoparticle 2 nm above the cover glass ($n = 1.52$). The simulated defocus curves are shown in figure 16. The simulation code can be found in [112].

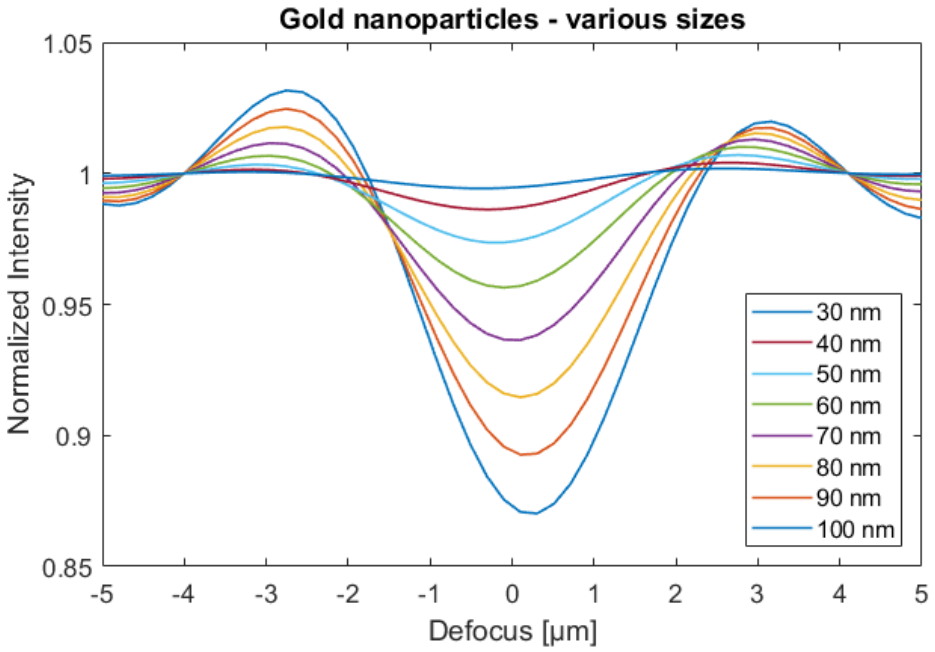

Figure 16: Simulated defocus curves of differently sized gold nanoparticles in our setup. The BEM simulations were done without a rotating sample illumination, and the reference light was not attenuated or phase shifted.

One can see in figure 16 that the nanoparticle contrast decreases rapidly when going to smaller sizes. Theoretically, this can be explained as the scattered field in equation (3) scales with the third power of the particle size, as outlined in section 2.2.1. For 30 nm gold nanoparticles, the contrast is already in the range of 10^{-3}. In order to be able to detect such small signals, other groups had to use a proper background subtraction scheme, which was often implemented by a dynamic imaging scheme [26].

To investigate which contrast range we could expect for single proteins in our setup, we simulated defocus curves of proteins (approximated as spheres with a refractive index of $n = 1.44$ [26] and sizes of 5-10 nm) in the same geometry as mentioned above. While we again decided not to simulate a rotating sample illumination, all protein simulations were done with an attenuation of the reference light ($T = 1.5 \cdot 10^{-4}$) and a phase shift of $\frac{\pi}{2}$ which corresponds to the specifications of our attenuator ring. The resulting defocus curves can be seen in figure 17. The BEM simulation code can be found in [112].

If we calculate the normalized intensity range (NI-range) of the simulated 10 nm protein, by subtracting the minimum value of its defocus curve from the maximum value, we get a NI-range of $4.6 \cdot 10^{-4}$ which is one order of magnitude smaller than the expected signal of a 30 nm gold nanoparticle.

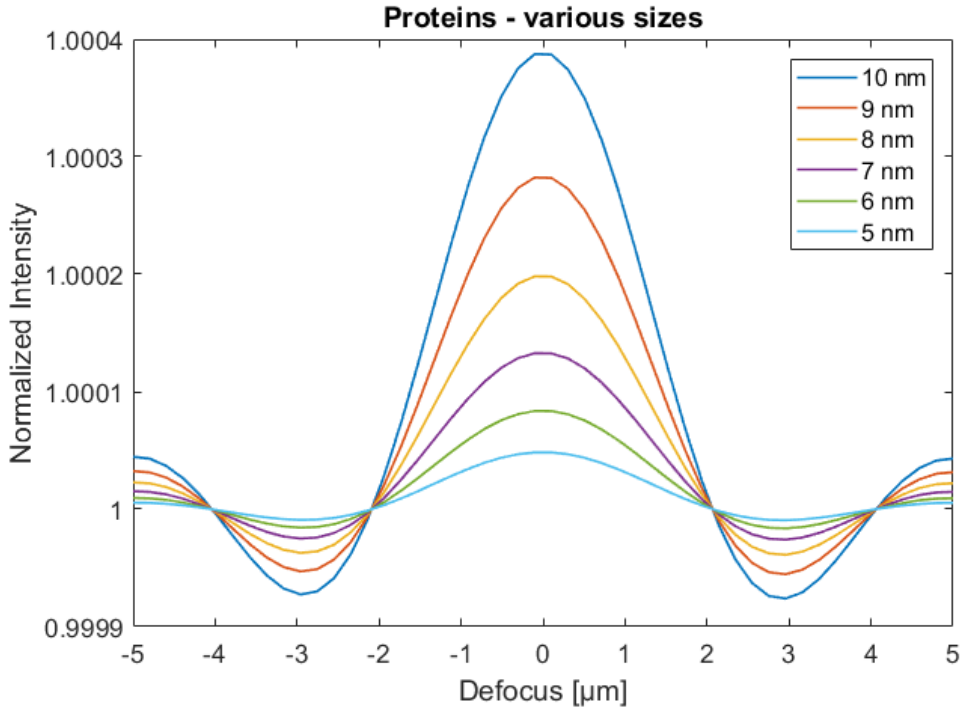

Figure 17: Simulated defocus curves of differently sized proteins (approximated as spheres with a refractive index of $n = 1.44$ [26]) in our setup. The BEM simulations were done without a rotating sample illumination. The reference light was attenuated ($T = 1.5 \cdot 10^{-4}$) and phase shifted by $\frac{\pi}{2}$.

If we compare simulations of a 10 nm protein with and without a phase shift of $\frac{\pi}{2}$ (but both times with attenuation), we can see in figure 18 that the phase shift ensures that we get an optimal contrast while still being in focus. This shows that the use of a phase shifter for the reference light, as it was suggested in section 2.3, is essential if the nanoparticle shall remain exactly in focus so that a precise re-imaging in the multi-passing scheme is possible.

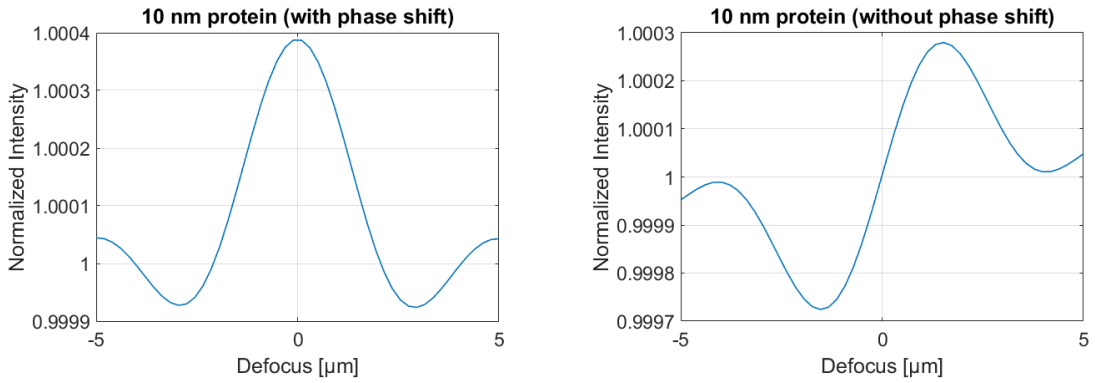

Figure 18: Simulated defocus curves of a 10 nm protein (approximated as spheres with a refractive index of $n = 1.44$ [26]) in our setup. The BEM simulations were done without a rotating sample illumination. Left: The reference light was phase shifted by $\frac{\pi}{2}$. Right: No phase shift of the reference light was used. An attenuation ($T = 1.5 \cdot 10^{-4}$) of the reference light was used for both simulations.

Simulating a 10 nm protein without attenuating the reference light is presented in figure 19. Comparing the simulated contrast values with attenuation (figure 17, in the range of 10^{-4}) and without attenuation of the reference light (figure 19, in the range of 10^{-6}) ensured us that the use of an attenuator will be vital for the detection of single proteins in our setup.

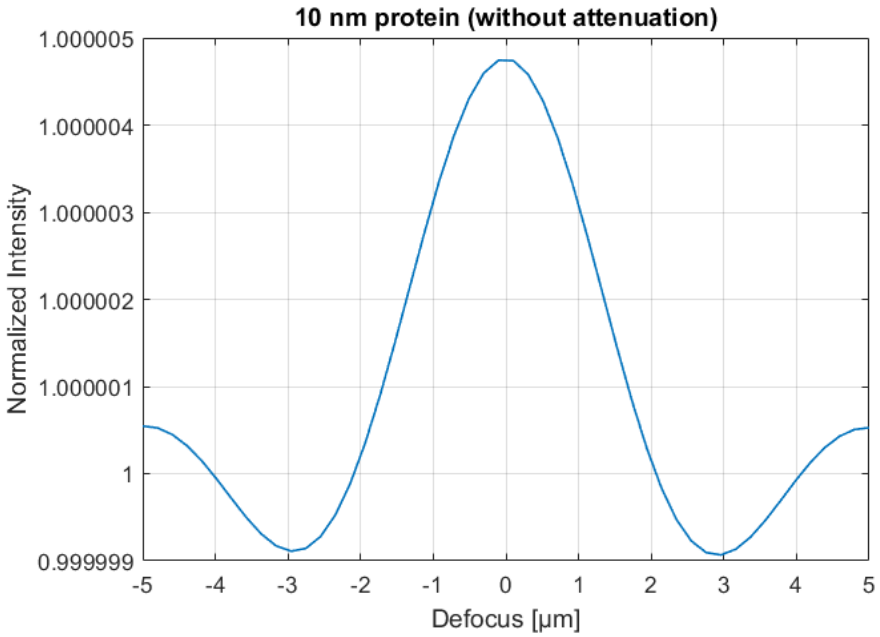

Figure 19: Simulated defocus curve of a 10 nm protein (approximated as a sphere with a refractive index of $n = 1.44$ [26]) without attenuation of the reference light in our setup. The BEM simulations were done without a rotating sample illumination but a phase shift ($\frac{\pi}{2}$) of the reference light was used.

In conclusion, our simulations showed that a contrast-detection sensitivity in the range of 10^{-4} is necessary to be able to detect single proteins with our microscope. To further investigate if this contrast sensitivity can be achieved with our setup, we performed a noise analysis of the microscope, which is presented in the next section.

3.5. Noise analysis

After simulating the expected contrast of smaller gold nanoparticles and proteins, we conducted a noise analysis of our setup to investigate on how long our microscope can be held stable. As outlined in chapter 2, it is vital to employ temporal binning in order to further improve the nanoparticle detection sensitivity after a proper background subtraction. Other groups needed to hold their setup stable long enough so that several hundreds or even thousands of frames could be averaged in order to reach a contrast sensitivity in the range of 10^{-4} [26]. As our simulated contrast values for a successful protein detection are in the same order of magnitude, our main goal was to investigate if our setup can also be held stable while acquiring several hundreds or thousands of frames.

But first, we focused on mechanical vibrations of the setup. Before conducting any measurements, we ensured that the setup is exposed to as little mechanical vibrations as possible by removing all unnecessary devices from the optical table, checking if the optical table is pumped properly, and making sure that the water cooling cables of the laser have no direct contact with the table. For the vibration measurements, we used a model 393B12 seismic ICP accelerometer from PCB Piezotronics. The signal from the sensor was analyzed (FFT) with an oscilloscope (MSOX3104T) from Keysight Technologies. The measured amplitudes of the FFT signal can be converted into acceleration values with a conversion factor of $1\frac{\mathrm{V}}{\mathrm{m/s^2}}$ which translates to displacements in the range of only a few nanometers for all presented measurements. However, such tiny displacements of optical elements can lead to severe optical path length variations if the orientation of the optical component, and thus the propagation angle of the light, is changed. Eventually, this can result in significant noise contributions.

The first mechanical vibration peaks we detected were around 80 and 150 Hz when placing the sensor onto the upper breadboard, which were caused by a fan that blows dry air into the laser resonator in order to prevent condensation on the optical components. As this condensation prevention is not required to run constantly, the fan can be temporarily deactivated if a stable setup is needed. The associated FFT signals can be seen in figure 31 and 32 in the appendix A.3. The fan was deactivated for all further measurements in this section.

Next, we checked if we could detect any mechanical vibrations on the different modules. When placing the sensor on the gimbal mount of the upper objective module, which is mounted in an overhanging configuration to a Thorlabs NanoMax stage (as can be seen in figure 7), we saw a clear peak around 50 Hz. A similar signal was detectable on the sample holder, which is also mounted in an overhanging configuration (as can be seen in figure 7). The associated FFT signals can be seen in figure 33 and 34 in the appendix A.3.

Measurements on the lower gimbal mount, which is placed on top (and in the middle) of an xy-stage, as can be seen in figure 7, led to no visible vibrations. The associated FFT signal can be seen in figure 35 in the appendix A.3.

If the sensor was placed onto the Thorlabs NanoMax stages' body (and not onto the overhanging gimbal mount or sample holder), there were also no vibrations detectable. Thus, we concluded that mounting the sample holder and the upper objective in an overhanging configuration was a poor design choice that is prone to mechanical vibrations. Suggestions on how to improve the mechanical stability of the setup are outlined in chapter 4.

Next, we analyzed how long our setup can be held stable during an image acquisition. Therefore, we turned off the condensation prevention fan and specified a region of interest of 256x256 pixels at the camera so that we could acquire images with a frame rate of 1354 frames per second. Moreover, we did not use a rotating sample illumination and covered the setup with the box that was presented in section 3.1.4. We imaged a dummy water sample between two cover glasses and acquired 2000 frames. For the analysis, we summed up frames and subtracted subsequent added frames, before normalizing the resulting expression. Then,

we calculated the standard deviation of all entries of the resulting matrix and plotted the standard deviation $\sigma(n)$ as a function of summed up frames n. Translated to an equation:

$$\sigma(n) = \mathrm{sd}_{2D}\left(\frac{\sum_{i=1}^{n} F_i - (\sum_{j=n+1}^{2n} F_j)}{\sum_{i=1}^{n} F_i + \sum_{j=n+1}^{2n} F_j}\right) \tag{15}$$

where sd_{2D} is the standard deviation of all matrix elements and F_i is the i-th frame. We compared our experimentally obtained noise values with the theoretical optimal behavior, i.e. the shot noise limit, according to equation (8). Note that the analysis was not done for all 256x256 pixels of the acquired frames, but only for a uniformly illuminated region of the frames (50x50 pixel), which was specified manually at the beginning of the analysis.

An initial test run of the analysis with no illumination light and the proper noise analysis of our microscope setup are shown in figure 20.

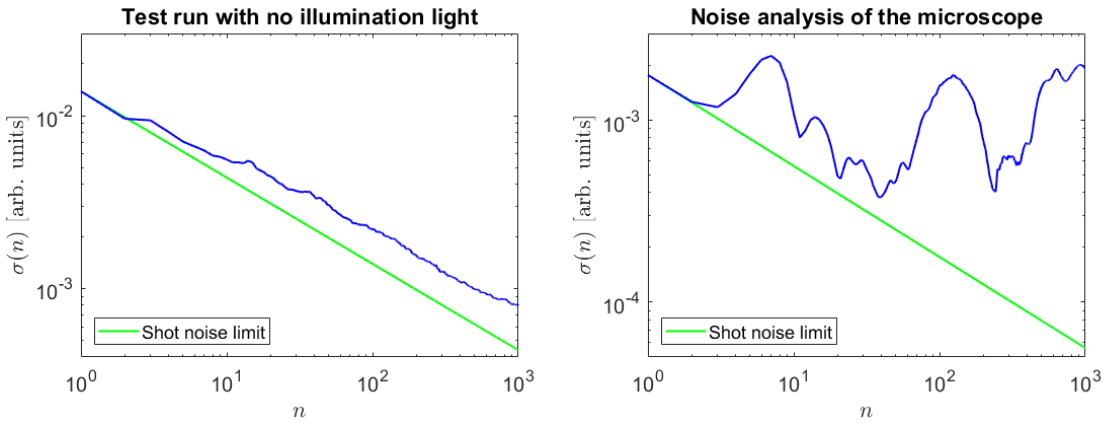

Figure 20: Test run of our noise analysis scheme with no illumination light (left) and noise analysis of the microscope setup (right). The standard deviation $\sigma(n)$ of summed up and normalized frames (according to equation (15)) is plotted against the number of summed up frames n. The shot noise limit (according to equation (8)) is shown in green.

In the test run without illumination light (figure 20 on the left), one can see that the calculated standard deviation stays close to the theoretical shot noise limit independent of the number of summed up frames, which is expected if no light, and thus no intensity variations, get captured by the camera, and which shows that the camera noise is statistically independent. Therefore, if all noise contributions are independent, we would ideally expect the noise to decrease as $\sqrt{n}$, where n is the number of summed up frames.

However, if the illumination light is switched on (figure 20 on the right), the calculated standard deviation is far from the optimal behavior, and increasing the number of summed up frames does not lead to a significant noise reduction. Thus, averaging over several hundreds or even thousands of frames and consequently reaching a contrast sensitivity of 10^{-4} with our setup seems unlikely. Possible consequences of the noise analysis are outlined in chapter 4.

3.6. Potential setup improvements

3.6.1. MP-iSCAT

Despite that the main effort should remain on increasing the mechanical stability of the setup and identifying other noise contributions, I would like to suggest some additional potential improvements of the setup for future upgrades: If the setup can only be held stable for short periods of time, a faster beam scanning speed for the rotating sample illumination will be required, which could be achieved with AODs. However, to get the same amount of frames in a shorter period of time, a camera with a higher frame rate would be required, which seems to be technically challenging in the foreseeable future. Increasing the illumination intensity to be able to capture the same amount of light during a shorter exposure time, on the other hand, should face no problems with our current light source.

Comparing the simulated defocus curves of a 10 nm protein with and without a phase shift of the reference light in figure 18 led us to the conclusion that a phase shift of $\frac{\pi}{2}$ is needed if the nanoparticle shall remain exactly in focus so that a precise re-imaging in our multi-passing scheme is possible. However, calculating the associated NI-ranges ($4.6 \cdot 10^{-4}$ with phase shift and $5.6 \cdot 10^{-4}$ without phase shift) reveals that an attenuator that does not alter the phase of the reference light would slightly increase the nanoparticle contrast. However, to profit from this contrast gain, one needs to acquire a defocus scan of the signal as the normalized intensity is equally distributed below and above one. For the signal with a phase shift, a defocus scan can also slightly increase the detectable contrast, but a majority of the signal can already be obtained if one manages to focus the microscope on the nanoparticle. Thus, using an attenuator without a phase shift of the reference light could increase the observed nanoparticle contrast, but the need for acquiring a defocus scan makes the image acquisition more complex, and it can be harder to find the nanoparticle signal in the first place, as the contrast, without changing the focus position, is lower than if a phase shift would be used.

During our design phase, we discarded the use of immersion objectives due to their significant lower transmission (compared to air objectives), which could overwhelm the contrast improvement gained by multi-passing if the photon loss negatively effects the SNR. However, simulations with an increased NA of 1.46, which can be achieved with oil immersion objectives that are commonly used in the iSCAT community [25, 26, 38], show that we could expect a single protein contrast improvement of a factor around 3. Thus, I suggest investigating if such a contrast improvement would compensate for the diminished improvement by the multi-passing due to a higher photon absorption rate if objectives with a higher NA are used in the setup.

Next, if keeping the focus position constant turns out to be problematic, which could be critical in particle tracking applications, a focus stabilization scheme, as discussed in section 2.2.5, could be implemented. Finally, switching to another illumination wavelength would

naturally improve the amount of scattered light for small nanoparticles as a consequence of Rayleigh scattering. Thus, employing an illumination wavelength that is more in the blue would also increase the observable nanoparticle contrast. However, a change of the illumination wavelength would require the exchange of almost all optical components, while the contrast of a single protein would only be improved by a modest factor of 2, according to our simulations.

3.6.2. MP-IRIS

In this final section, I would like to discuss an idea for a new imaging scheme that we came across when thinking about redesigning our setup to improve its mechanical stability. In the new scheme, the sample is placed directly onto a mirror, which means the microscope can be operated without the need for an upper objective module, an upper tube lens module, and an upper end mirror module. This would significantly simplify the setup and give more space, physically and mentally, to ensure that the remaining components can be redesigned in the most stable way possible. Moreover, the detection path would be positioned directly on the optical table, which should further improve the stability of the setup.

Our proposed imaging scheme is very similar to the SP-IRIS scheme [48, 49] with the key difference that we are using a mirror instead of an imaging sensor which allows us to re-image the reference and scattered light back onto the sample multiple times. Thus, our proposed scheme can still be seen as a multi-passing scheme, and hence I would like to call it multi-pass interferometric reflection imaging scheme (MP-IRIS).

For successfully directing the outcoupled light[35] towards the camera, the detection path would be situated where the alignment tool is positioned in our current setup. In order to redirect all the light that has interacted with the sample towards the detection path, a combination of a polarizing beam splitter and a quarter-wave plate can be used. The attenuator can again be positioned at a Fourier plane in the detection path[36]. If the quarter-wave plate is placed inside the self-imaging cavity, all light that has interacted with the sample will be directed towards the detection path at the polarizing beam splitter, while the back-reflected illumination light from the end mirror will propagate back in the direction towards the laser where it can be blocked. However, that presupposes that the quarter-wave plate has a very high transmission. Moreover, introducing an additional optical component will always make the alignment process of the self-imaging cavity more difficult.

If the quarter-wave plate is positioned outside the self-imaging cavity, i.e. before the end mirror, the back-reflected illumination light from the end mirror will also be directed towards the detection path. This is problematic as the scattered light would be overwhelmed with the back-reflected illumination light. As the back-reflected illumination light is significantly stronger than the actual reference and scattered light, it would also easily saturate our camera.

[35] The light is outcoupled at the lower end mirror in the MP-IRIS.

[36] The setup would then look similar to the one in [39] where they use a partial reflector as an attenuator in the detection path.

Thus, the only option to successfully operate the microscope with a quarter wave-plate outside the self-imaging cavity would be to constantly operate the Pockels cell with an appropriate timing so that only the light that has interacted with the sample is directed towards the camera which is possible as we are working with pulsed illumination. The multi-passing scheme, which involves directing a specific pass or multiple passes towards the camera, could be operated similarly as in the current setup.

To investigate what nanoparticle contrast we could expect in the MP-IRIS, we adapted our BEM simulations, which are outlined in section 2.4, for the proposed imaging scheme. As our code already supported the use of layered media, we only had to implement a Fresnel thin film calculation which could correctly simulate the amplitude and phase of the reference light, after it gets reflected at the mirror material which has a complex refractive index. This was achieved by implementing 'jreftran - A layered thin film transmission and reflection coefficient calculator' by Shawn Divitt [120]. Our code can be found in [112].

We decided to use silver ($n_{silver} = 0.05 + 3.2\mathrm{i}$) as a mirror material in our simulations as it has a reflectivity of over 97 % for our illumination wavelength ($\lambda = 517.5$ nm) and combine it with a protective layer of SiO_2 ($n_{oxide} = 1.46$) on top of it, similar to how the IRIS is designed in [48, 49]. The refractive indices were obtained from [118]. The protective layer thickness can now be chosen so that the interference of the backward scattered light and the reflection of the forward scattered light is maximized for our illumination wavelength [48, 49]. For this, we simulated the expected NI-ranges of a 10 nm single protein ($n = 1.44$ [26]) as a function of the protective layer thickness. In order to be able to properly compare the new simulations with the simulations of the MP-iSCAT scheme, we again placed the protein 2 nm above the protective layer, simulated the same attenuator (with $T = 1.5 \cdot 10^{-4}$ and a phase shift of $\frac{\pi}{2}$) and set the refractive index of the surrounding medium to the refractive index of water ($n = 1.33$). No rotating sample illumination was used to keep the simulations comparable. The result of the expected NI-range simulations as a function of the protective layer thickness can be found in figure 21. A defocus curve of the protein with the optimized layer thickness of 60 nm, according to the results in figure 21, is shown in figure 22.

With an optimized layer thickness of 60 nm, a NI-range of $2.8 \cdot 10^{-3}$ can be achieved with the MP-IRIS, which is a factor of 6 better than the simulated NI-range of a same-sized protein in MP-iSCAT ($4.6 \cdot 10^{-4}$ from figure 17). This signal enhancement is in good agreement with fluorescent studies on a layered silver mirror in [121][37]. The superior contrast can be explained when considering that in a transmission scheme (like MP-iSCAT), only the forward scattered light can be captured by the camera. In MP-IRIS, on the contrary, not only the reflected forward scattered light, but also the backward scattered light can be captured. Thus, the backward scattered light and the reflected forward scattered light can constructively interfere,

[37] Note that the contrast in iSCAT, according to equation (3), scales with the scattered field strength and not with the scattered intensity. Thus, the ~30x intensity enhancement in [121] corresponds to a ~5.5x field strength enhancement.

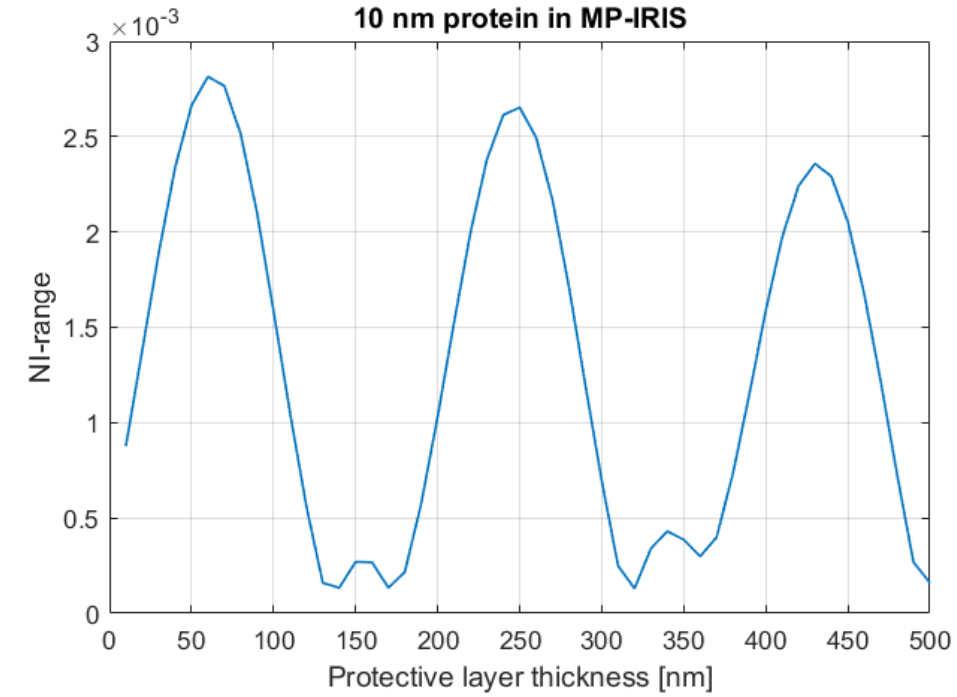

Figure 21: Simulated normalized intensity ranges (NI-ranges) of a 10 nm protein (approximated as a sphere with a refractive index of $n = 1.44$ [26]) for different protective layer thicknesses in the MP-IRIS. The BEM simulations were done without a rotating sample illumination. The reference light was attenuated ($T = 1.5 \cdot 10^{-4}$) and phase shifted by $\frac{\pi}{2}$.

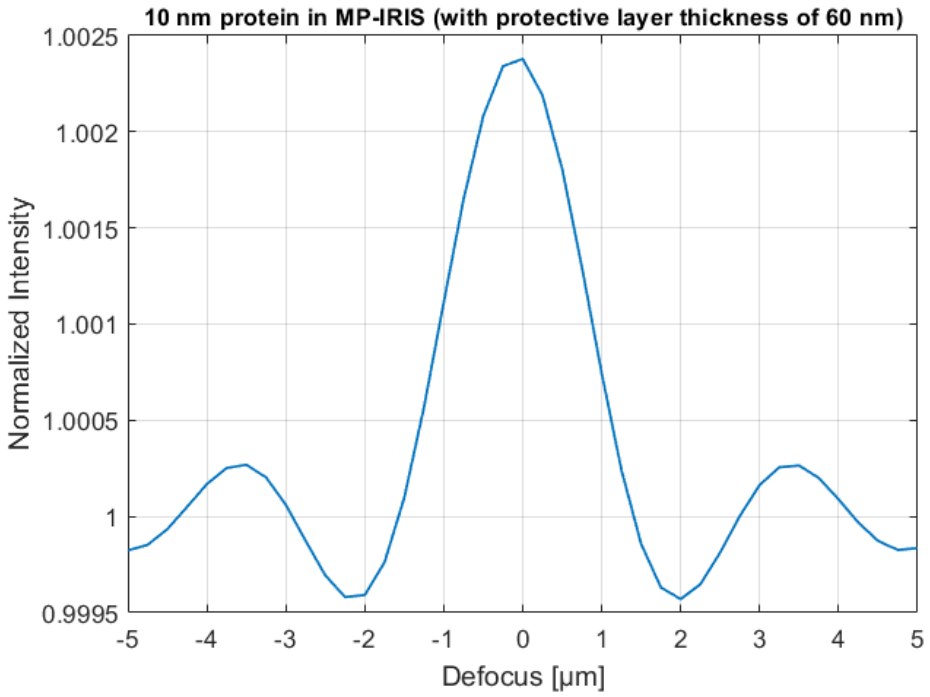

Figure 22: Simulated defocus curve of a 10 nm protein (approximated as a sphere with a refractive index of $n = 1.44$ [26]) with an optimized protective layer thickness of 60 nm in the MP-IRIS. The BEM simulations were done without a rotating sample illumination. The reference light was attenuated ($T = 1.5 \cdot 10^{-4}$) and phase shifted by $\frac{\pi}{2}$.

which enhances the amount of scattered light in the detection direction if the protective layer thickness is chosen accordingly [48, 49]. An illustration of the detectable scattered light in MP-iSCAT and MP-IRIS is shown in figure 23. Furthermore, the illumination light intensity can get amplified at the nanoparticle due to constructive self-interference in the form of a standing light wave as a result of the reflection at the mirror, which additionally contributes to an increased amount of scattered light.

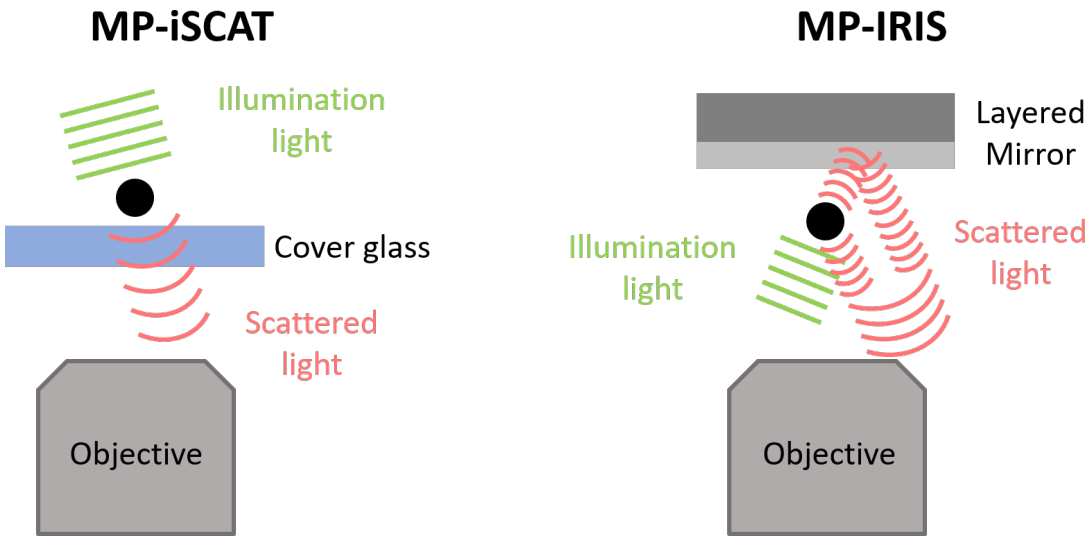

Figure 23: Illustration of the collectable scattered light in MP-iSCAT (left) and the MP-IRIS (right). While in MP-iSCAT, only the forward scattered light can be detected, the reflected forward scattered and the backscattered light can be captured in the MP-IRIS. For a constructive interference of the reflected forward scattered and the backscattered light in the MP-IRIS, an appropriate protective layer thickness at the mirror must be chosen.

As discussed above, the signal in the MP-IRIS is mainly enhanced because the backward scattered and reflected forward scattered light are constructively interfering if the protective layer thickness is chosen accordingly. The forward scattered and reflected light traverses the protective layer two times and together with a phase shift around π at the reflection, the forward scattered and reflected light can interfere constructively with the backscattered light if a layer thickness of $\widetilde{\lambda}/4$ is selected, where $\widetilde{\lambda} = \lambda/n_{oxide}$ [49].

We think that the reason why the simulated layer thickness (60 nm) does not precisely match the calculated value of $\widetilde{\lambda}/4 = 89$ nm, is mainly that the reflection at the mirror, which takes place inside the SiO_2 layer, does not produce an exact phase shift of π but rather a phase shift of $229°$ for light that hits the mirror perpendicularly, according to a calculation with [120]. Moreover, not all light is scattered so that it hits the mirror perpendicularly. Hence, most of the scattered light traverses longer paths inside the protective layer, which naturally leads to a decreased simulated layer thickness.

If the MP-IRIS is further pursued, one should investigate which materials are best suited for the protective layer, regarding manufacturing feasibility, cost, surface roughness, cleanability, and protein binding behavior, and repeat the protective layer thickness simulations with the

best candidates. Silver, on the other hand, already seems to be the best choice as a mirror material, as it has a high reflectivity at our illumination wavelength and is commonly used as a mirror material, which should make the final mirror affordable and easy to produce. Suggestions on how to properly manufacture a layered silver mirror can, for example, be found in [121].

The simulated contrast of a 10 nm protein does only differ by a factor of 1.1 in MP-iSCAT when comparing a simulation with the use of a rotating sample illumination (with an illumination angle that is compatible with our attenuator ring) and a simulation where no rotating sample illumination was used. However, in the MP-IRIS, the two simulated contrast values differ by a factor of 2, which implies that a restriction of the illumination NA is more important in the MP-IRIS. A possible explanation for this is that the layered mirror is designed for constructive interference of the backscattered and forward scattered light if low-NA illumination light is used [48]. However, one can simply reduce the amplitude of the rotating sample illumination and employ the designed dot attenuator if it turns out that a rotating sample illumination together with the attenuator ring decreases the nanoparticle contrast excessively.

Including or excluding a $\frac{\pi}{2}$ phase shift of the reference light in the MP-IRIS simulations shows the same behavior as outlined in section 3.4.3. Thus, the conclusion made in section 3.6.1 also remains the same, i.e. an attenuator that does not alter the phase would slightly increase the observed nanoparticle contrast, but on the other hand, it would also complicate the detection process, for the MP-IRIS. Finally, the mentioned potential use of an immersion objective with a higher NA of 1.46 in section 3.6.1 also shows an increased single protein contrast by a factor of 2.5 in the MP-IRIS, according to our simulations. Thus, I would similarly suggest investigating if such a contrast improvement would compensate for the diminished improvement by the multi-passing due to a higher photon absorption rate, if an objective with a higher NA is used in the MP-IRIS.

4. Conclusion

In the course of this thesis, we successfully designed, developed, and tested an interferometric multi-pass microscope with a rotating sample illumination. We could demonstrate a working multi-passing scheme, and with the low light loss rate of 8 % per roundtrip, we were able to detect light that has interacted with the sample 19 times. Furthermore, we could show that interferometric multi-pass imaging of gold nanoparticles obtains a better contrast than single-pass imaging as a proof-of-concept experiment. Additionally, we successfully implemented BEM simulations of our interferometric imaging scheme and validated them by comparing simulated defocus curves of gold nanoparticles with experimentally obtained defocus curves. Further BEM simulations showed that we can expect a detectable contrast of single proteins in our setup if our designed attenuator ring will be used. However, it will be vital to further work on an efficient background subtraction, potentially implemented as a dynamic imaging scheme.

The conducted noise analysis revealed that further improvements of the setup are necessary for a single protein detection in the future. Based on the vibration measurements, we concluded that mounting critical (optical) components, like the objectives and the sample stage, in an overhanging configuration was a poor design choice that is prone to mechanical vibrations. Therefore, it seems to be unavoidable to at least redesign the sample module and the upper objective module. If a redesign is conducted, it is probably the smartest choice to redesign the whole setup to improve its mechanical stability. This could be achieved by decreasing the size of the upper breadboard (and/or supporting it better) or changing to a completely different way of setting up the vertical part of the microscope. A configuration where the (optical) components are mounted in the middle of stable stages, which are connected to the optical table with four posts, seems to be a good option to minimize mechanical vibrations. This claim is supported by our vibration measurements of the lower objective module, which is mounted in a stable configuration as mentioned in the previous sentence, and the setups of other iSCAT groups who are capable of imaging single proteins [101].

Nevertheless, further noise investigations are needed, especially to find out if the mechanical vibrations are causing our limited long-time stability when acquiring multiple hundreds or thousands of frames for a temporal binning scheme. Identifying and quantifying the contribution of other noise sources, for example laser intensity fluctuations, also seems necessary.

Switching from our implemented imaging scheme (MP-iSCAT) to the newly presented multi-pass interferometric reflection imaging scheme (MP-IRIS) seems promising as our simulations suggest an increased protein contrast in the MP-IRIS. Even more important, in my opinion, is that the setup in the MP-IRIS needs fewer optical components. Thus, a smaller vertical section of the microscope, compared to MP-iSCAT, is required. This should make it possible to construct an overall improved setup in regard to mechanical stability. Both advantages together make it appealing to consider switching to a MP-IRIS.

Based on the findings of this thesis, the suggestions mentioned above on how to further optimize or redesign the setup will hopefully lead the way for future interferometric multi-pass imaging of single proteins with our microscope. The increased nanoparticle contrast due to the multi-passing scheme could eventually even allow the detection of smaller proteins than currently achievable in other iSCAT setups. Ultimately, I hope that our efforts will one day result in new insights into microscopic processes, which could potentially lead to numerous applications in molecular biology and biomedical research.

5. Acknowledgement

At this last point, I have to "misuse our terminology to thank those who interfered constructively to make this thesis possible" [122].

First of all, I would like to thank my supervisor Thomas Juffmann for giving me the opportunity to work on this thesis. Moreover, I am deeply grateful for all the discussions we had together, his advice and help whenever needed. Next, I would like to thank Clara Conrad-Billroth for working on the microscope together with me, letting me use her lunch card and all the fruitful discussions we had. I would also like to thank all members of the Quantum Imaging and Biophysics group, in chronological order Marius, Dante, Philipp, Matthias, Ilia, and Raphael, who helped to keep our laboratory running, mainly by making sure that enough Lab Snacks are available at all times, and with whom I enjoyed countless lunch hours and the occasional social events after a long day at work.

A special 'thank you' is also directed to Derin Sevenler, who formerly worked in the SP-IRIS community, for sharing his BEM simulation code with us and answering many questions of mine.

Due to the global SARS-CoV-2 outbreak, most of the writing for this thesis has happened in home quarantine, which turned out to be quite tedious and emotionally isolating. Luckily, I could count on virtual contact with friends of mine, especially Sebastian, Max, Magda, and Lisa, to whom I want to express my deep gratitude for supporting me during these challenging times.

Schlussendlich möchte ich mich bei meinen Eltern und Großeltern für ihre lebenslange Unterstützung bedanken! Ohne ihre Ermutigung meiner Neugierde von Kindheit an und ohne ihre emotionale und finanzielle Unterstützung wäre mein Physikstudium, und die damit verbundene Masterarbeit, nie möglich gewesen.

References

[1] W. Chiu. "What Does Electron Cryomicroscopy Provide that X-Ray Crystallography and NMR Spectroscopy Cannot?" In: *Annual Review of Biophysics and Biomolecular Structure* 22.1 (1993), pp. 233–255. URL: https://doi.org/10.1146/annurev.bb.22.060193.001313.

[2] K. Lindorff-Larsen et al. "Simultaneous determination of protein structure and dynamics". In: *Nature* 433.7022 (2005), pp. 128–132. URL: https://doi.org/10.1038/nature03199.

[3] J. Lippincott-Schwartz, E. Snapp, and A. Kenworthy. "Studying protein dynamics in living cells". In: *Nature Reviews Molecular Cell biology* 2.6 (2001), pp. 444–456. URL: https://doi.org/10.1038/35073068.

[4] J. Andrecka et al. "Structural dynamics of myosin 5 during processive motion revealed by interferometric scattering microscopy". In: *Elife* 4 (2015), e05413. URL: https://doi.org/10.7554/eLife.05413.

[5] W. E. Moerner and D. P. Fromm. "Methods of single-molecule fluorescence spectroscopy and microscopy". In: *Review of Scientific Instruments* 74.8 (2003), pp. 3597–3619. URL: https://doi.org/10.1063/1.1589587.

[6] S. Shashkova and M. C. Leake. "Single-molecule fluorescence microscopy review: shedding new light on old problems". In: *Bioscience Reports* 37.4 (2017), BSR20170031. URL: https://doi.org/10.1042/BSR20170031.

[7] F. Zernike. "Phase contrast, a new method for the microscopic observation of transparent objects". In: *Physica* 9.7 (1942), pp. 686–698. URL: https://doi.org/10.1016/S0031-8914(42)80035-X.

[8] G. Popescu. *Quantitative Phase Imaging of Cells and Tissues*. McGraw-Hill, 2011. ISBN: 978-0-07-166342-7.

[9] M. Renz. "Fluorescence microscopy—A historical and technical perspective". In: *Cytometry Part A* 83.9 (2013), pp. 767–779. URL: https://doi.org/10.1002/cyto.a.22295.

[10] D. Gerlach. *Geschichte der Mikroskopie*. Harri Deutsch, 2009, pp. 625–657. ISBN: 9783817117819.

[11] O. Heimstädt. "Das Fluoreszenzmikroskop". In: *Zeitschrift für wissenschaftliche Mikroskopie und mikroskopische Technik* 28 (1911), pp. 330–337.

[12] H. Lehmann. *Das Luminszenz-Mikroskop: seine Grundlagen und seine Anwendungen*. 1913.

[13] P. Ellinger and A. Hirt. "Mikroskopische Untersuchungen an lebenden Organen". In: *Archiv für experimentelle Pathologie und Pharmakologie* 145 (1929), pp. 193–210.

[14] J. W. Lichtman and J. Conchello. "Fluorescence microscopy". In: *Nature Methods* 2 (2005), pp. 910–919. URL: https://doi.org/10.1038/nmeth817.

[15] R. Y. Tsien. "The green fluorescent protein". In: *Annual Review of Biochemistry* 67.1 (1998), pp. 509–544. URL: https://doi.org/10.1146/annurev.biochem.67.1.509.

[16] D. C. Prasher et al. "Primary structure of the *Aequorea victoria* green-fluorescent protein". In: *Gene* 111.2 (1992), pp. 229–233. URL: https://doi.org/10.1016/0378-1119(92)90691-H.

[17] M. Chalfie et al. "Green fluorescent protein as a marker for gene expression". In: *Science* 263.5148 (1994), pp. 802–805. URL: https://doi.org/10.1126/science.8303295.

[18] L. Möckl, D. C. Lamb, and C. Bräuchle. "Super-resolved Fluorescence Microscopy: Nobel Prize in Chemistry 2014 for Eric Betzig, Stefan Hell, and William E. Moerner". In: *Angewandte Chemie International Edition* 53.51 (2014), pp. 13972–13977. URL: https://doi.org/10.1002/anie.201410265.

[19] W. E. Moerner and L. Kador. "Optical detection and spectroscopy of single molecules in a solid". In: *Physical Review Letters* 62 (1989), pp. 2535–2538. URL: https://doi.org/10.1103/PhysRevLett.62.2535.

[20] E. Betzig et al. "Imaging Intracellular Fluorescent Proteins at Nanometer Resolution". In: *Science* 313.5793 (2006), pp. 1642–1645. URL: https://doi.org/10.1126/science.1127344.

[21] T. A. Klar, E. Engel, and S. W. Hell. "Breaking Abbe's diffraction resolution limit in fluorescence microscopy with stimulated emission depletion beams of various shapes". In: *Physical Review E* 64 (2001), p. 066613. URL: https://doi.org/10.1103/PhysRevE.64.066613.

[22] J. Ortega Arroyo, D. Cole, and P. Kukura. "Interferometric scattering microscopy and its combination with single-molecule fluorescence imaging". In: *Nature Protocols* 11.4 (2016), pp. 617–633. URL: https://doi.org/10.1038/nprot.2016.022.

[23] R. M. Dickson et al. "On/off blinking and switching behaviour of single molecules of green fluorescent protein". In: *Nature* 388.6640 (1997), pp. 355–358. URL: https://doi.org/10.1038/41048.

[24] R. W. Taylor and V. Sandoghdar. "Interferometric Scattering (iSCAT) Microscopy and Related Techniques". In: *Label-Free Super-Resolution Microscopy*. Ed. by V. Astratov. Springer International Publishing, 2019, pp. 25–65. ISBN: 978-3-030-21722-8. URL: https://doi.org/10.1007/978-3-030-21722-8_2.

[25] J. Ortega Arroyo et al. "Label-Free, All-Optical Detection, Imaging, and Tracking of a Single Protein". In: *Nano Letters* 14.4 (2014), pp. 2065–2070. URL: https://doi.org/10.1021/nl500234t.

[26] M. Piliarik and V. Sandoghdar. "Direct optical sensing of single unlabelled proteins and super-resolution imaging of their binding sites". In: *Nature Communications* 5 (2014), p. 4495. URL: https://doi.org/10.1038/ncomms5495.

[27] G. Young et al. "Quantitative mass imaging of single biological macromolecules". In: *Science* 360.6387 (2018), pp. 423–427. URL: https://doi.org/10.1126/science.aar5839.

[28] K. Lindfors et al. "Detection and Spectroscopy of Gold Nanoparticles Using Supercontinuum White Light Confocal Microscopy". In: *Physical Review Letters* 93 (2004), p. 037401. URL: https://doi.org/10.1103/PhysRevLett.93.037401.

[29] P. Kukura et al. "High-speed nanoscopic tracking of the position and orientation of a single virus". In: *Nature Methods* 6.12 (2009), pp. 923–927. URL: https://doi.org/10.1038/nmeth.1395.

[30] G. Young and P. Kukura. "Interferometric Scattering Microscopy". In: *Annual Review of Physical Chemistry* 70.1 (2019), pp. 301–322. URL: https://doi.org/10.1146/annurev-physchem-050317-021247.

[31] V. Jacobsen et al. "Interferometric optical detection and tracking of very small gold nanoparticles at a water-glass interface". In: *Optics Express* 14.1 (2006), pp. 405–414. URL: https://doi.org/10.1364/OPEX.14.000405.

[32] H. Ewers et al. "Label-Free Optical Detection and Tracking of Single Virions Bound to Their Receptors in Supported Membrane Bilayers". In: *Nano Letters* 7.8 (2007), pp. 2263–2266. URL: https://doi.org/10.1021/nl070766y.

[33] R. W. Taylor et al. "Interferometric scattering microscopy reveals microsecond nanoscopic protein motion on a live cell membrane". In: *Nature Photonics* 13 (2019), pp. 480–487. URL: https://doi.org/10.1038/s41566-019-0414-6.

[34] M. P. McDonald et al. "Visualizing Single-Cell Secretion Dynamics with Single-Protein Sensitivity". In: *Nano Letters* 18.1 (2017), pp. 513–519. URL: https://doi.org/10.1021/acs.nanolett.7b04494.

[35] R. F. Garmann, A. M. Goldfain, and V. N. Manoharan. "Measurements of the self-assembly kinetics of individual viral capsids around their RNA genome". In: *Proceedings of the National Academy of Sciences* 116.45 (2019), pp. 22485–22490. URL: https://doi.org/10.1073/pnas.1909223116.

[36] A. M. Goldfain et al. "Dynamic Measurements of the Position, Orientation, and DNA Content of Individual Unlabeled Bacteriophages". In: *The Journal of Physical Chemistry B* 120.26 (2016), pp. 6130–6138. URL: https://doi.org/10.1021/acs.jpcb.6b02153.

[37] J.-S. Park et al. "Label-free and live cell imaging by interferometric scattering microscopy". In: *Chemical Science* 9.10 (2018), pp. 2690–2697. URL: https://doi.org/10.1039/C7SC04733A.

[38] C.-Y. Cheng, Y.-H. Liao, and C.-L. Hsieh. "High-speed imaging and tracking of very small single nanoparticles by contrast enhanced microscopy". In: *Nanoscale* 11.2 (2019), pp. 568–577. URL: https://doi.org/10.1039/C8NR06789A.

[39] D. Cole et al. "Label-Free Single-Molecule Imaging with Numerical-Aperture-Shaped Interferometric Scattering Microscopy". In: *ACS Photonics* 4.2 (2017), pp. 211–216. URL: https://doi.org/10.1021/acsphotonics.6b00912.

[40] Y.-F. Huang et al. "Coherent Brightfield Microscopy Provides the Spatiotemporal Resolution To Study Early Stage Viral Infection in Live Cells". In: *ACS Nano* 11.3 (2017), pp. 2575–2585. URL: https://doi.org/10.1021/acsnano.6b05601.

[41] Y.-F. Huang et al. "Label-free, ultrahigh-speed, 3D observation of bidirectional and correlated intracellular cargo transport by coherent brightfield microscopy". In: *Nanoscale* 9.19 (2017), pp. 6567–6574. URL: https://doi.org/10.1039/C7NR00604G.

[42] C.-L. Hsieh. "Label-free, ultrasensitive, ultrahigh-speed scattering-based interferometric imaging". In: *Optics Communications* 422 (2018), pp. 69 –74. URL: https://doi.org/10.1016/j.optcom.2018.02.058.

[43] W. Li et al. "Direct Optical Visualization of Graphene and Its Nanoscale Defects on Transparent Substrates". In: *Nano Letters* 16.8 (2016), pp. 5027–5031. URL: https://doi.org/10.1021/acs.nanolett.6b01804.

[44] G. G. Daaboul et al. "LED-based interferometric reflectance imaging sensor for quantitative dynamic monitoring of biomolecular interactions". In: *Biosensors and Bioelectronics* 26.5 (2011), pp. 2221–2227. URL: https://doi.org/10.1016/j.bios.2010.09.038.

[45] O. Avci et al. "Interferometric Reflectance Imaging Sensor (IRIS)—A Platform Technology for Multiplexed Diagnostics and Digital Detection". In: *Sensors* 15.7 (2015), pp. 17649–17665. URL: https://doi.org/10.3390/s150717649.

[46] J. T. Trueb et al. "Robust Visualization and Discrimination of Nanoparticles by Interferometric Imaging". In: *IEEE Journal of Selected Topics in Quantum Electronics* 23.2 (2016), pp. 394–403. URL: https://doi.org/10.1109/JSTQE.2016.2639824.

[47] D. Sevenler et al. "Digital Microarrays: Single-Molecule Readout with Interferometric Detection of Plasmonic Nanorod Labels". In: *ACS Nano* 12.6 (2018), pp. 5880–5887. URL: https://doi.org/10.1021/acsnano.8b02036.

[48] D. Sevenler, O. Avci, and M. S. Ünlü. "Quantitative interferometric reflectance imaging for the detection and measurement of biological nanoparticles". In: *Biomedical Optics Express* 8.6 (2017), pp. 2976–2989. URL: https://doi.org/10.1364/BOE.8.002976.

[49] O. Avci et al. "Pupil function engineering for enhanced nanoparticle visibility in wide-field interferometric microscopy". In: *Optica* 4.2 (2017), pp. 247–254. URL: https://doi.org/10.1364/OPTICA.4.000247.

[50] C. Théry, M. Ostrowski, and E. Segura. "Membrane vesicles as conveyors of immune responses". In: *Nature Reviews Immunology* 9.8 (2009), pp. 581–593. URL: https://doi.org/10.1038/nri2567.

[51] J. Zhang et al. "Exosome and Exosomal MicroRNA: Trafficking, Sorting, and Function". In: *Genomics, Proteomics & Bioinformatics* 13.1 (2015), pp. 17 –24. URL: https://doi.org/10.1016/j.gpb.2015.02.001.

[52] G. G. Daaboul et al. "Digital Detection of Exosomes by Interferometric Imaging". In: *Scientific Reports* 6 (2016), p. 37246. URL: https://doi.org/10.1038/srep37246.

[53] G. G. Daaboul et al. "High-Throughput Detection and Sizing of Individual Low-Index Nanoparticles and Viruses for Pathogen Identification". In: *Nano Letters* 10.11 (2010), pp. 4727–4731. URL: https://doi.org/10.1021/nl103210p.

[54] S. M. Scherr et al. "Real-Time Capture and Visualization of Individual Viruses in Complex Media". In: *ACS Nano* 10.2 (2016), pp. 2827–2833. URL: https://doi.org/10.1021/acsnano.5b07948.

[55] G. G. Daaboul et al. "Enhanced light microscopy visualization of virus particles from Zika virus to filamentous ebolaviruses". In: *PLoS One* 12.6 (2017), e0179728. URL: https://doi.org/10.1371/journal.pone.0179728.

[56] Z. Wang et al. "Spatial light interference microscopy (SLIM)". In: *Optics Express* 19.2 (2011), pp. 1016–1026. URL: https://doi.org/10.1364/OE.19.001016.

[57] D. Gabor. "A New Microscopic Principle". In: *Nature* 161 (1948), pp. 777–778. URL: https://www.nature.com/articles/161777a0.

[58] R. Wang et al. "Dispersion-relation phase spectroscopy of intracellular transport". In: *Optics Express* 19.21 (2011), pp. 20571–20579. URL: https://doi.org/10.1364/OE.19.020571.

[59] M. E. Kandel et al. "Label-Free Imaging of Single Microtubule Dynamics Using Spatial Light Interference Microscopy". In: *ACS Nano* 11.1 (2017), pp. 647–655. URL: https://doi.org/10.1021/acsnano.6b06945.

[60] H. Majeed et al. "Label-free quantitative evaluation of breast tissue using Spatial Light Interference Microscopy (SLIM)". In: *Scientific Reports* 8 (2018), p. 6875. URL: https://doi.org/10.1038/s41598-018-25261-7.

[61] L. Limozin and K. Sengupta. "Quantitative Reflection Interference Contrast Microscopy (RICM) in Soft Matter and Cell Adhesion". In: *ChemPhysChem* 10.16 (2009), pp. 2752–2768. URL: https://doi.org/10.1002/cphc.200900601.

[62] Y.-H. Lin, W.-L. Chang, and C.-L. Hsieh. "Shot-noise limited localization of single 20 nm gold particles with nanometer spatial precision within microseconds". In: *Optics Express* 22.8 (2014), pp. 9159–9170. URL: https://doi.org/10.1364/OE.22.009159.

[63] F. Jünger, P. v. Olshausen, and A. Rohrbach. "Fast, label-free super-resolution live-cell imaging using rotating coherent scattering (ROCS) microscopy". In: *Scientific Reports* 6 (2016), p. 30393. URL: https://doi.org/10.1038/srep30393.

[64] M. Liebel, J. T. Hugall, and N. F. van Hulst. "Ultrasensitive Label-Free Nanosensing and High-Speed Tracking of Single Proteins". In: *Nano Letters* 17.2 (2017), pp. 1277–1281. URL: https://doi.org/10.1021/acs.nanolett.6b05040.

[65] Y. Yang et al. "Interferometric plasmonic imaging and detection of single exosomes". In: *Proceedings of the National Academy of Sciences* 115.41 (2018), pp. 10275–10280. URL: https://doi.org/10.1073/pnas.1804548115.

[66] M. Delor et al. "Imaging material functionality through three-dimensional nanoscale tracking of energy flow". In: *Nature Materials* 19.1 (2020), pp. 56–62. URL: https://doi.org/10.1038/s41563-019-0498-x.

[67] M. Fox. *Quantum Optics: An Introduction*. Oxford University Press, 2006, p. 81. ISBN: 0191524255.

[68] T. Juffmann et al. "Multi-pass microscopy". In: *Nature Communications* 7.1 (2016), p. 12858. URL: https://doi.org/10.1038/ncomms12858.

[69] S. Nimmrichter et al. "Full-field cavity enhanced microscopy techniques". In: *Journal of Physics: Photonics* 1.1 (2018), p. 015007. URL: https://doi.org/10.1088/2515-7647/aae228.

[70] V. Giovannetti, S. Lloyd, and L. Maccone. "Advances in quantum metrology". In: *Nature Photonics* 5.4 (2011), pp. 222–229. URL: https://doi.org/10.1038/nphoton.2011.35.

[71] V. Giovannetti, S. Lloyd, and L. Maccone. "Quantum Metrology". In: *Physical Review Letters* 96.1 (2006), p. 010401. URL: https://doi.org/10.1103/PhysRevLett.96.010401.

[72] A. Luis. "Phase-shift amplification for precision measurements without nonclassical states". In: *Physical Review A* 65.2 (2002), p. 025802. URL: https://doi.org/10.1103/PhysRevA.65.025802.

[73] B. L. Higgins et al. "Entanglement-free Heisenberg-limited phase estimation". In: *Nature* 450.7168 (2007), pp. 393–396. URL: https://doi.org/10.1038/nature06257.

[74] V. Giovannetti, S. Lloyd, and L. Maccone. "Quantum-Enhanced Measurements: Beating the Standard Quantum Limit". In: *Science* 306.5700 (2004), pp. 1330–1336. URL: https://doi.org/10.1126/science.1104149.

[75] Y. Israel, S. Rosen, and Y. Silberberg. "Supersensitive Polarization Microscopy Using NOON States of Light". In: *Physical Review Letters* 112.10 (2014), p. 103604. URL: https://doi.org/10.1103/PhysRevLett.112.103604.

[76] T. Ono, R. Okamoto, and S. Takeuchi. "An entanglement-enhanced microscope". In: *Nature Communications* 4.1 (2013), p. 2326. URL: https://doi.org/10.1038/ncomms3426.

[77] M. A. Taylor et al. "Biological measurement beyond the quantum limit". In: *Nature Photonics* 7.3 (2013), pp. 229–233. URL: https://doi.org/10.1038/nphoton.2012.346.

[78] G. Brida, M. Genovese, and I. R. Berchera. "Experimental realization of sub-shot-noise quantum imaging". In: *Nature Photonics* 4.4 (2010), pp. 227–230. URL: https://doi.org/10.1038/nphoton.2010.29.

[79] N. Friis et al. "Flexible resources for quantum metrology". In: *New Journal of Physics* 19.6 (2017), p. 063044. URL: https://doi.org/10.1088/1367-2630/aa7144.

[80] M. Mader et al. "A scanning cavity microscope". In: *Nature Communications* 6.1 (2015), p. 7249. URL: https://doi.org/10.1038/ncomms8249.

[81] N. C. Pégard and J. W. Fleischer. "Contrast Enhancement by Multi-Pass Phase-Conjugation Microscopy". In: *CLEO:2011 - Laser Applications to Photonic Applications*. Optical Society of America, 2011, CThW6. URL: https://doi.org/10.1364/CLEO_SI.2011.CThW6.

[82] B. B. Klopfer, T. Juffmann, and M. A. Kasevich. "Multi-pass phase microscopy". In: *Optics in the Life Sciences Congress*. Optical Society of America, 2017, NS1C.5. URL: https://doi.org/10.1364/NTM.2017.NS1C.5.

[83] B. B. Klopfer, T. Juffmann, and M. A. Kasevich. "Iterative creation and sensing of twisted light". In: *Optics Letters* 41.24 (2016), pp. 5744–5747. URL: https://doi.org/10.1364/OL.41.005744.

[84] T. Juffmann et al. "Multi-pass transmission electron microscopy". In: *Scientific Reports* 7.1 (2017), p. 1699. URL: https://doi.org/10.1038/s41598-017-01841-x.

[85] B. Buscher et al. "Bioanalysis for plasma protein binding studies in drug discovery and drug development: views and recommendations of the European Bioanalysis Forum". In: *Bioanalysis* 6.5 (2014), pp. 673–682. URL: https://doi.org/10.4155/bio.13.338.

[86] M. L. Howard et al. "Plasma Protein Binding in Drug Discovery and Development". In: *Combinatorial Chemistry & High Throughput Screening* 13.2 (2010), pp. 170–187. URL: https://doi.org/10.2174/138620710790596745.

[87] J. K. Willmann et al. "Molecular imaging in drug development". In: *Nature Reviews Drug Discovery* 7.7 (2008), pp. 591–607. URL: https://doi.org/10.1038/nrd2290.

[88] G. J. Kelloff and C. C. Sigman. "Cancer biomarkers: selecting the right drug for the right patient". In: *Nature Reviews Drug Discovery* 11.3 (2012), pp. 201–214. URL: https://doi.org/10.1038/nrd3651.

[89] E. Abbe. "Beiträge zur Theorie des Mikroskops und der mikroskopischen Wahrnehmung". In: *Archiv für mikroskopische Anatomie* 9 (1873), pp. 413 –468. URL: http://publikationen.ub.uni-frankfurt.de/frontdoor/index/index/year/2009/docId/11525.

[90] L. G. Gouy. "Sur une propriété nouvelles des ondes lumineuses". In: *C. R. Acad. Sci. Paris* 110 (1890), pp. 1251–1253.

[91] R. W. Boyd. "Intuitive explanation of the phase anomaly of focused light beams". In: *Journal of the Optical Society of America* 70.7 (1980), pp. 877–880. URL: https://doi.org/10.1364/JOSA.70.000877.

[92] S. Feng and H. G. Winful. "Physical origin of the Gouy phase shift". In: *Optics Letters* 26.8 (2001), pp. 485–487. URL: https://doi.org/10.1364/OL.26.000485.

[93] J. Mertz. *Introduction to Optical Microscopy*. Roberts and Company Publishers, 2010, pp. 189–190. ISBN: 978-09815194-8-7.

[94] C. F. Bohren and D. R. Huffman. *Absorption and Scattering of Light by Small Particles*. Wiley-VCH, 1998. ISBN: 978-0-471-29340-8.

[95] C. F. Bohren and D. R. Huffman. *Absorption and Scattering of Light by Small Particles*. Wiley-VCH, 1998, pp. 139–148. ISBN: 978-0-471-29340-8.

[96] R. W. Taylor and V. Sandoghdar. "Interferometric Scattering Microscopy: Seeing Single Nanoparticles and Molecules via Rayleigh Scattering". In: *Nano Letters* 19.8 (2019), pp. 4827–4835. URL: https://doi.org/10.1021/acs.nanolett.9b01822.

[97] D. Sevenler. "Development of a digitalmicroarray with interferometric reflectance imaging". PhD thesis. Boston University, 2017. URL: https://hdl.handle.net/2144/27008.

[98] T. Latychevskaia. "Lateral and axial resolution criteria in incoherent and coherent optics and holography, near- and far-field regimes". In: *Applied Optics* 58.13 (2019), pp. 3597–3603. URL: https://doi.org/10.1364/AO.58.003597.

[99] E. Abbe. "Beiträge zur Theorie des Mikroskops und der mikroskopischen Wahrnehmung". In: *Archiv für mikroskopische Anatomie* 9 (1873), p. 456. URL: http://publikationen.ub.uni-frankfurt.de/frontdoor/index/index/year/2009/docId/11525.

[100] J. Mertz. *Introduction to Optical Microscopy*. Roberts and Company Publishers, 2010, pp. 36–40. ISBN: 978-09815194-8-7.

[101] A. Gemeinhardt et al. "Label-Free Imaging of Single Proteins Secreted from Living Cells via iSCAT Microscopy". In: *JoVE (Journal of Visualized Experiments)* 141 (2018), e58486. URL: https://doi.org/10.3791/58486.

[102] J. Ortega-Arroyo and P. Kukura. "Interferometric scattering microscopy (iSCAT): new frontiers in ultrafast and ultrasensitive optical microscopy". In: *Physical Chemistry Chemical Physics* 14.45 (2012), pp. 15625–15636. URL: https://doi.org/10.1039/C2CP41013C.

[103] P. Kukura et al. "Single-Molecule Sensitivity in Optical Absorption at Room Temperature". In: *The Journal of Physical Chemistry Letters* 1.23 (2010), pp. 3323–3327. URL: https://doi.org/10.1021/jz101426x.

[104] M. Celebrano et al. "Single-molecule imaging by optical absorption". In: *Nature Photonics* 5.2 (2011), pp. 95–98. URL: https://doi.org/10.1038/nphoton.2010.290.

[105] E. Posner. *Shot noise generator*. https://github.com/erezposner/Shot-Noise-Generator. GitHub repository, commit 4fbcc6e8cd4236b66f2bb3a672e9ff599c270f41. 2019.

[106] C.-L. Hsieh et al. "Tracking Single Particles on Supported Lipid Membranes: Multimobility Diffusion and Nanoscopic Confinement". In: *The Journal of Physical Chemistry B* 118.6 (2014), pp. 1545–1554. URL: https://doi.org/10.1021/jp412203t.

[107] C.-Y. Cheng and C.-L. Hsieh. "Background Estimation and Correction for High-Precision Localization Microscopy". In: *ACS Photonics* 4.7 (2017), pp. 1730–1739. URL: https://doi.org/10.1021/acsphotonics.7b00238.

[108] M. G. Hyeon et al. "Reflection Phase Microscopy by Successive Accumulation of Interferograms". In: *ACS Photonics* 6.3 (2019), pp. 757–766. URL: https://doi.org/10.1021/acsphotonics.8b01703.

[109] A. J. Bowman et al. "Electro-optic imaging enables efficient wide-field fluorescence lifetime microscopy". In: *Nature Communications* 10.1 (2019), p. 4561. URL: https://doi.org/10.1038/s41467-019-12535-5.

[110] U. Hohenester and A. Trügler. "MNPBEM - A Matlab toolbox for the simulation of plasmonic nanoparticles". In: *Computer Physics Communications* 183.2 (2012), pp. 370 –381. URL: https://doi.org/10.1016/j.cpc.2011.09.009.

[111] D. Sevenler, O. Avci, and M. S. Ünlü. *SP-IRIS-BEM*. https://github.com/derinsevenler/SP-IRIS-BEM/. GitHub repository, commit fa2b6b192df700608dac898604f1a56ba14c60aa. 2017.

[112] J. Pac and T. Juffmann. *MP-iSCAT-BEM*. https://github.com/jannis357/MP-iSCAT-BEM/. GitHub repository, commit 9114bc5518261b705f74e6cd2c86e133f9ad3ff4. 2020.

[113] F. J. García de Abajo and A. Howie. "Retarded field calculation of electron energy loss in inhomogeneous dielectrics". In: *Physical Review B* 65.11 (2002), p. 115418. URL: https://doi.org/10.1103/PhysRevB.65.115418.

[114] L. Novotny and B. Hecht. *Principles of Nano-Optics*. 2nd ed. Cambridge University Press, 2012. ISBN: 978-1-107-00546-4.

[115] J. Peatross and M. Ware. *Physics of Light and Optics*. Brigham Young University, 2019, p. 291. ISBN: 978-1-312-92927-2. URL: https://optics.byu.edu/BYUOpticsBook_2015.pdf.

[116] S. J. Byrnes. "Multilayer optical calculations". In: *arXiv preprint arXiv:1603.02720* (2016). URL: https://arxiv.org/abs/1603.02720.

[117] G. Boisset. *Luxpop thin film calculator*. http://www.luxpop.com/HU_v174.cgi?OpCode=69. Accessed on 13th June 2019.

[118] M. N. Polyanskiy. *Refractive index database*. https://refractiveindex.info. Accessed on 13th June 2019.

[119] O. Avci et al. "Physical modeling of interference enhanced imaging and characterization of single nanoparticles". In: *Optics Express* 24.6 (2016), pp. 6094–6114. URL: https://doi.org/10.1364/OE.24.006094.

[120] S. Divitt. *jreftran - A layered thin film transmission and reflection coefficient calculator*. MATLAB Central File Exchange, version from 15 Nov 2016. https://de.mathworks.com/matlabcentral/fileexchange/50923-jreftran-a-layered-thin-film-transmission-and-reflection-coefficient-calculator.

[121] E. Le Moal et al. "Enhanced Fluorescence Cell Imaging with Metal-Coated Slides". In: *Biophysical Journal* 92.6 (2007), pp. 2150 –2161. URL: https://doi.org/10.1529/biophysj.106.096750.

[122] T. K. Juffmann. "Surface based detection schemes for molecular matter wave interferometry". PhD thesis. Universität Wien, 2012, p. 105. URL: http://othes.univie.ac.at/25837/.

A. Appendix

A.1. Final SolidWorks modules and associated adapters

This section of the appendix shows the final modules and the associated adapters, which were developed in SolidWorks, as outlined in section 3.1.4. The final lower end mirror module and the associated adapter are shown in figure 24. Figure 25 shows the final lower tube lens module where the same adapter as in figure 24 is used.

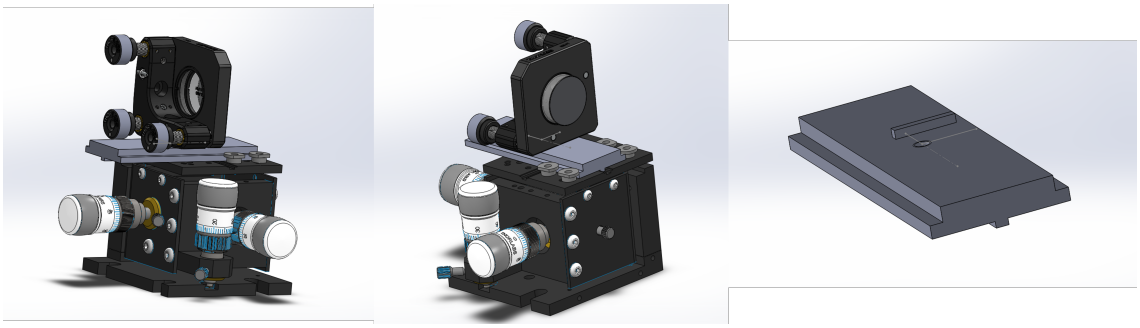

Figure 24: Left and middle: Lower end mirror module consisting of MicroBlock stage (MBT616D/M), mirror mount (KS1T) and custom-designed adapter. Right: Adapter to connect the stage and the mirror mount.

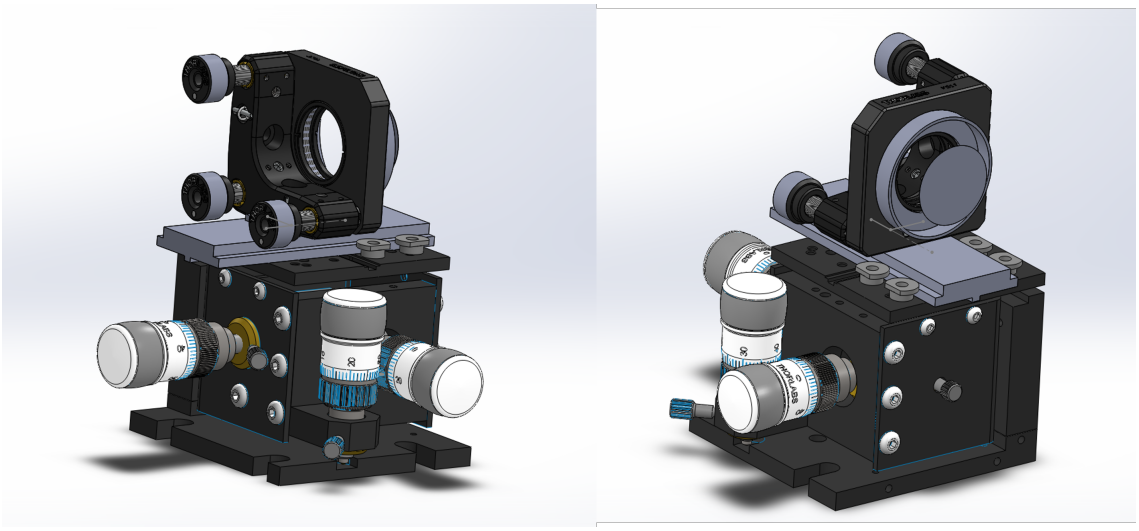

Figure 25: Lower tube lens module consisting of MicroBlock stage (MBT616D/M), mirror mount (KS1T) and custom-designed adapter. The same adapter as shown in figure 24 is used.

The upper end mirror and tube lens modules (and the associated adapter) are shown in figure 26 and 27. Note that the adapters for the upper modules shift the end mirror and the tube lens by a half-hole spacing in the transverse direction because the breadboard is offset by a half-hole spacing due to the position of the counterbored holes that are used to connect the breadboard to the optical table. The half-hole offset can be seen in figure 5.

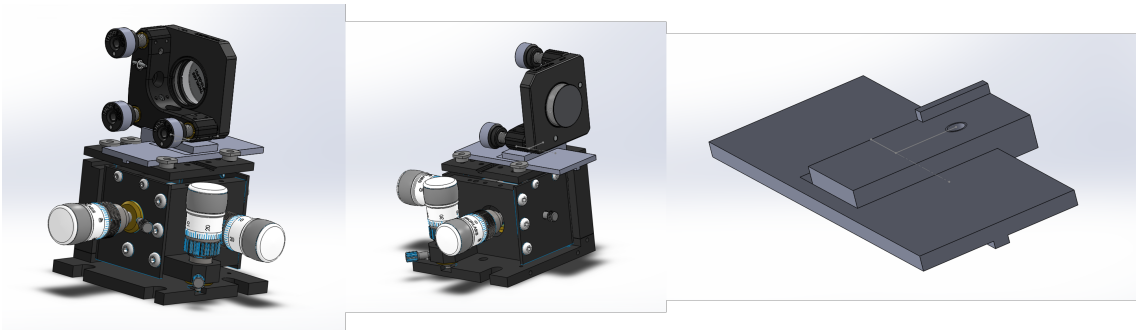

Figure 26: Left and middle: Upper end mirror module consisting of MicroBlock stage (MBT616D/M), mirror mount (KS1T) and custom-designed adapter. Right: Adapter to connect the stage and the mirror mount.

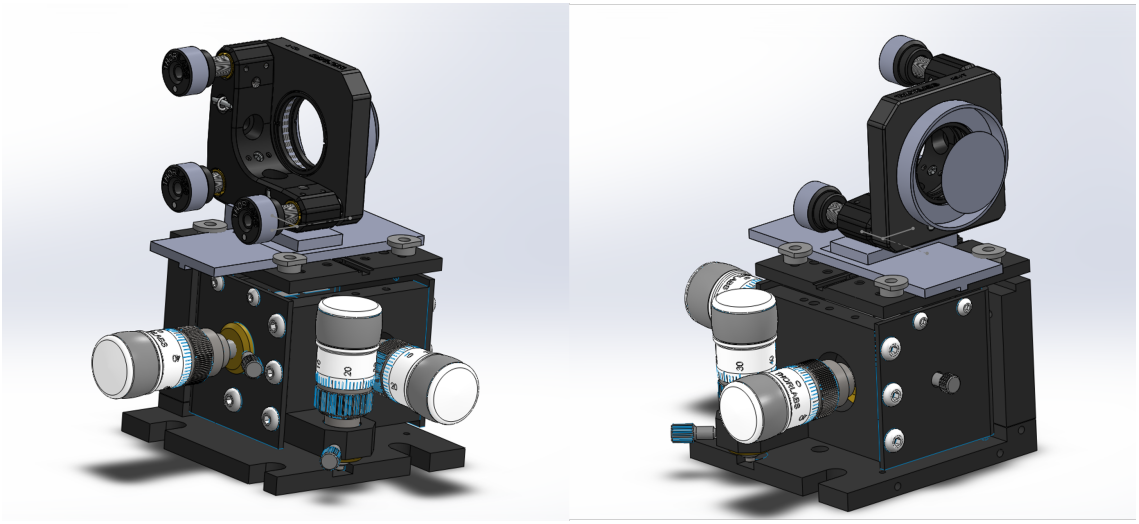

Figure 27: Upper tube lens module consisting of MicroBlock stage (MBT616D/M), mirror mount (KS1T) and custom-designed adapter. The same adapter as shown in figure 26 is used.

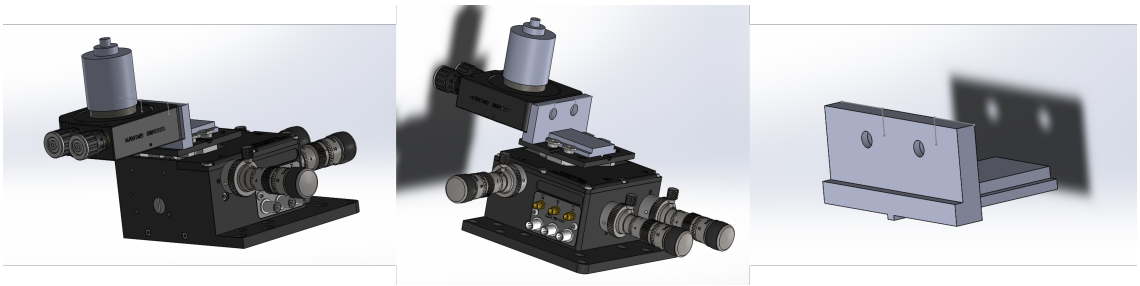

Figure 28: Left and middle: Lower objective module consisting of NanoMax stage (MAX311D/M), gimbal mirror mount (GM100/M) and custom-designed adapter. Right: Adapter to connect the stage and the gimbal mirror mount.

The lower and upper objective modules with their respective adapters are shown in figure 28 and 29.

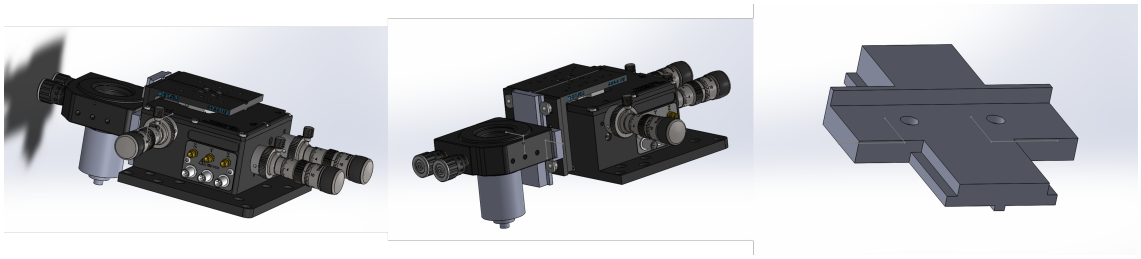

Figure 29: Left and middle: Upper objective module consisting of NanoMax stage (MAX311D/M) with changed top plate (AMA011/M), gimbal mirror mount (GM100/M) and custom-designed adapter. Right: Adapter to connect the stage and the gimbal mirror mount.

A.2. Noise isolation box

This section of the appendix shows the final noise isolation box, which was developed in SolidWorks to shield the microscope from ambient light, air movements and to dampen acoustic noise, as outlined in section 3.1.4. The complete multi-pass setup together with the box (without the side and top panels) can be seen in figure 30. The box is clamped to the optical table when in use.

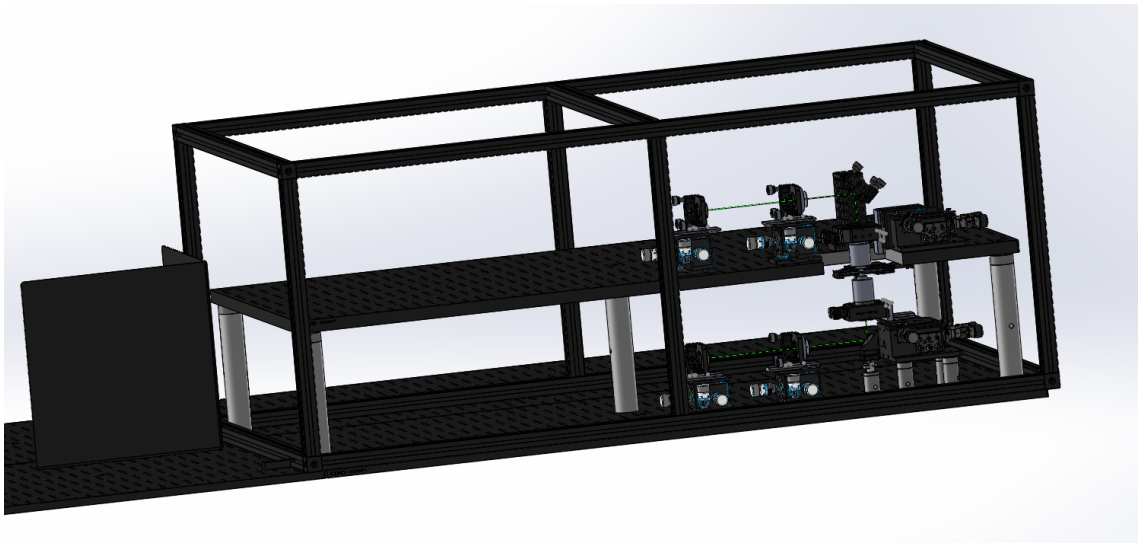

Figure 30: Box (without side and top panels) covering the multi-pass setup to shield the microscope from ambient light, air movements and to dampen acoustic noise.

A.3. FFT signals of the vibration measurements

This section of the appendix shows the FFT signals of our conducted vibration measurements, as outlined in section 3.5.

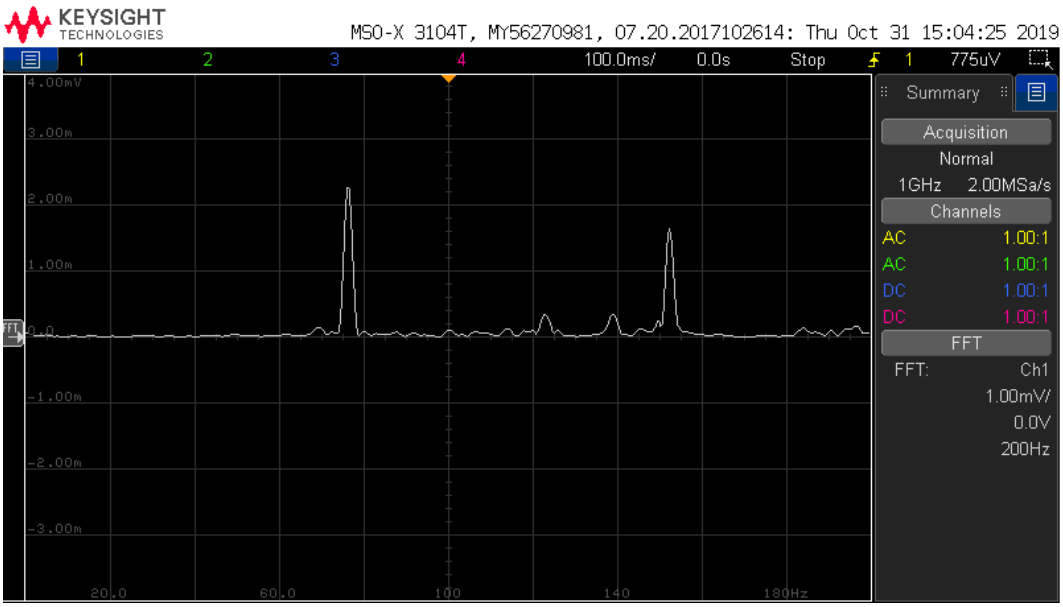

Figure 31: FFT of the seismic accelerometer signal if the condensation prevention fan is on. The accelerometer was placed on the upper breadboard.

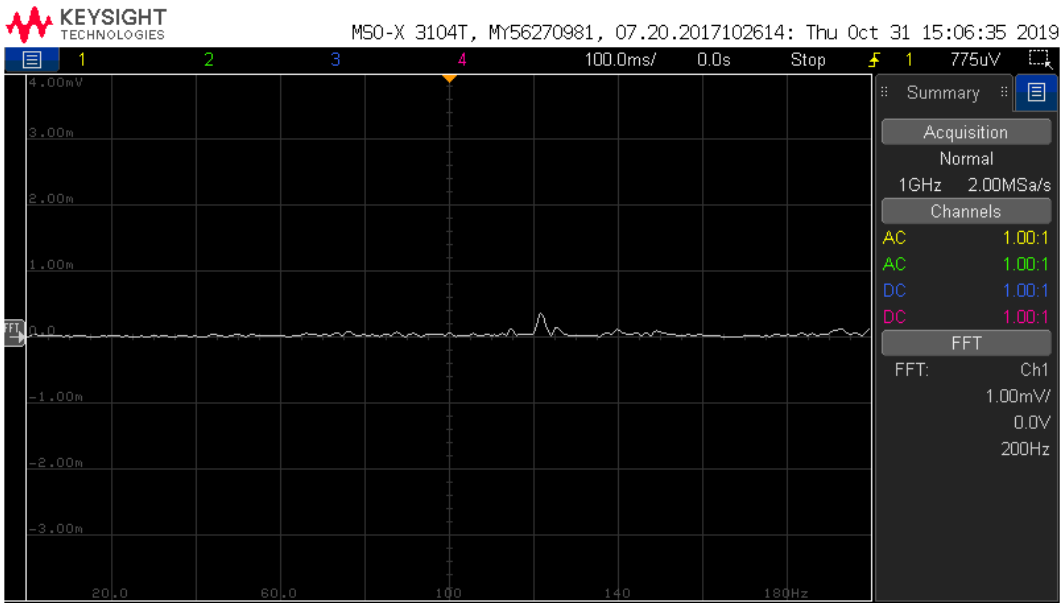

Figure 32: FFT of the seismic accelerometer signal if the condensation prevention fan is off. The accelerometer was placed on the upper breadboard.

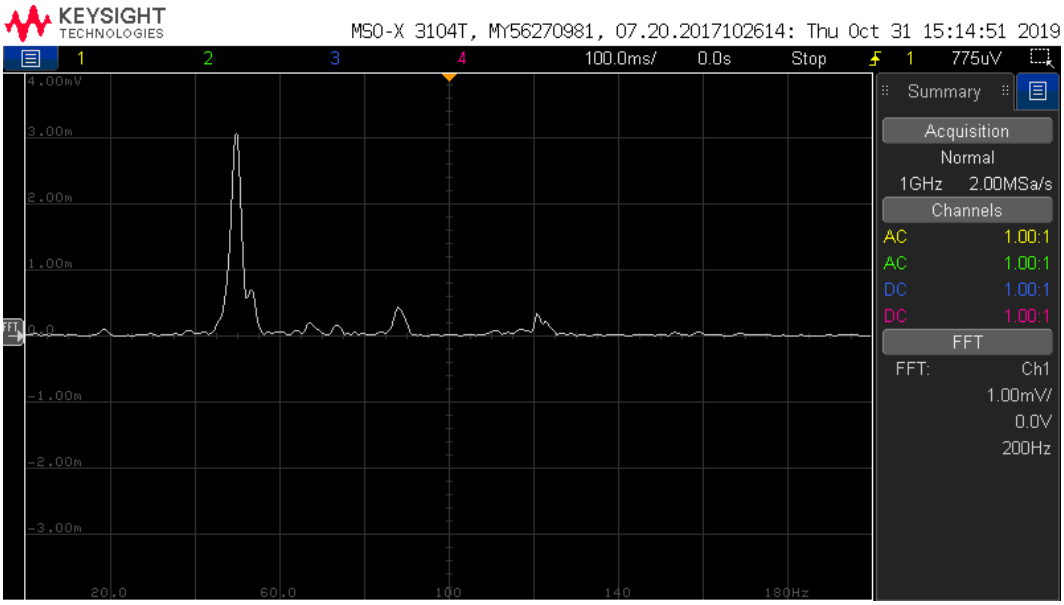

Figure 33: FFT of the seismic accelerometer signal when placing it onto the gimbal mount of the upper objective module which is mounted to a Thorlabs NanoMax stage in an overhanging configuration (shown in figure 7).

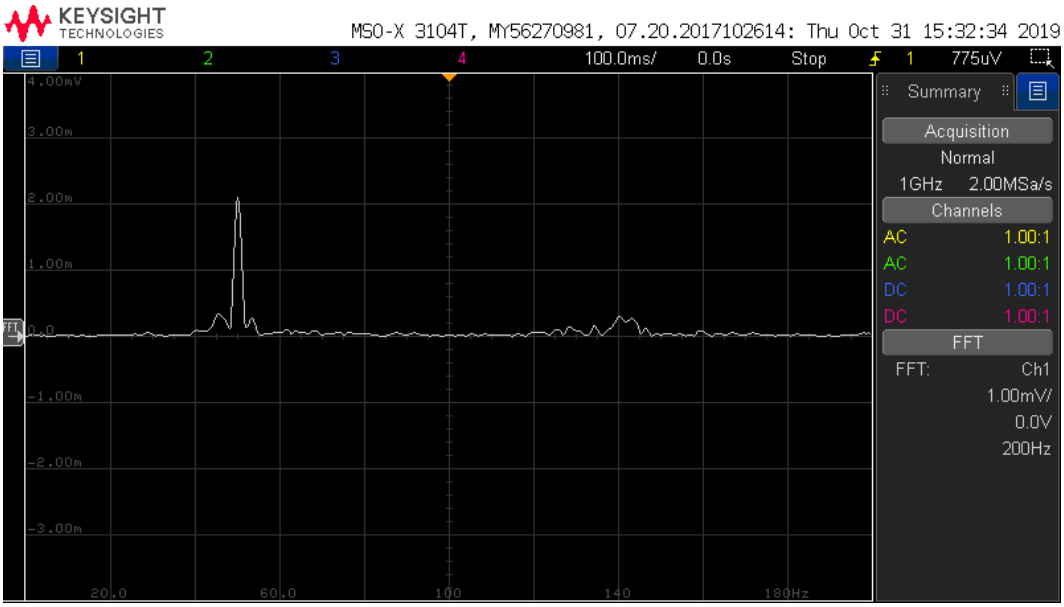

Figure 34: FFT of the seismic accelerometer signal when placing it onto the sample holder which is mounted in an overhanging configuration (shown in figure 7).

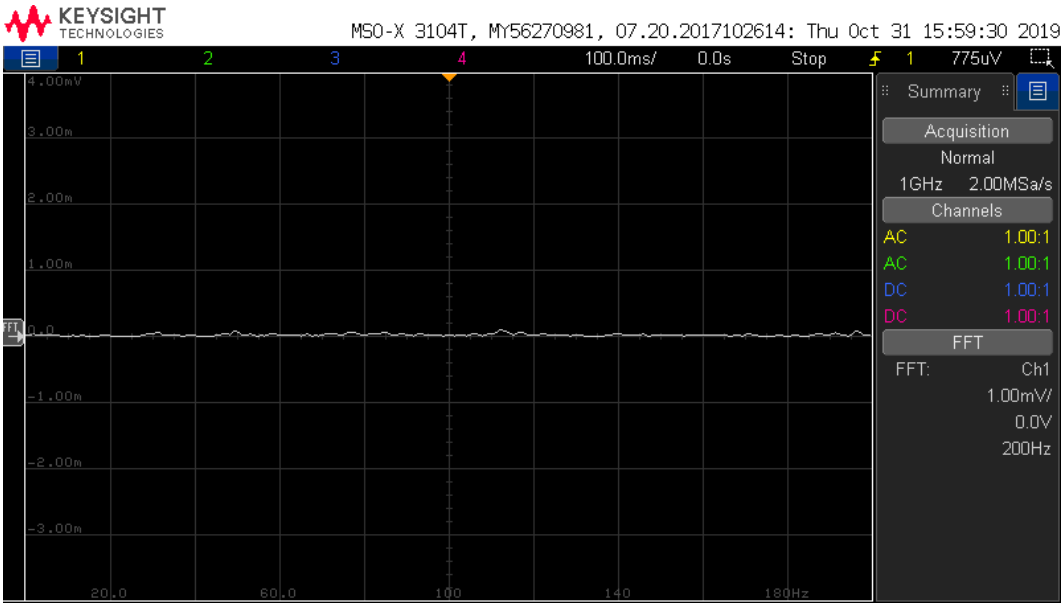

Figure 35: FFT of the seismic accelerometer signal when placing it onto the gimbal mount of the lower objective module which is mounted on top (and in the middle) of an xy-stage (shown in figure 7).